

# Linking Chemical Electron–Proton Transfer to Proton Pumping in Cytochrome *c* Oxidase: Broken-Symmetry DFT Exploration of Intermediates along the Catalytic Reaction Pathway of the Iron–Copper Dinuclear Complex

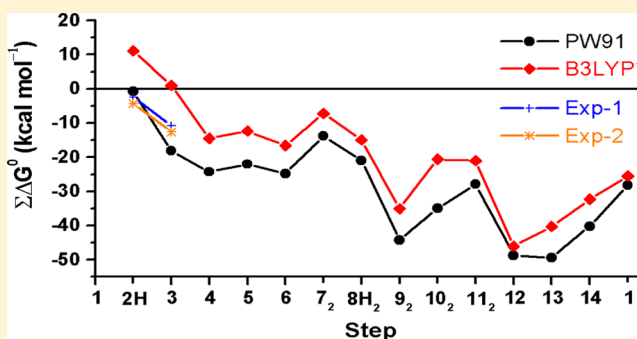
Louis Noodleman,<sup>\*,†</sup> Wen-Ge Han Du,<sup>†</sup> James A. Fee,<sup>†</sup> Andreas W. Götz,<sup>‡</sup> and Ross C. Walker<sup>‡,§</sup>

<sup>†</sup>Department of Integrative Structural and Computational Biology, The Scripps Research Institute, 10550 North Torrey Pines Road, TPC15, La Jolla, California 92037, United States

<sup>‡</sup>San Diego Supercomputer Center and <sup>§</sup>Department of Chemistry and Biochemistry, University of California at San Diego, 9500 Gilman Drive, MC0505, La Jolla, California 92093, United States

## S Supporting Information

**ABSTRACT:** After a summary of the problem of coupling electron and proton transfer to proton pumping in cytochrome *c* oxidase, we present the results of our earlier and recent density functional theory calculations for the dinuclear Fe–a<sub>3</sub>–Cu<sub>B</sub> reaction center in this enzyme. A specific catalytic reaction wheel diagram is constructed from the calculations, based on the structures and relative energies of the intermediate states of the reaction cycle. A larger family of tautomers/protonation states is generated compared to our earlier work, and a new lowest-energy pathway is proposed. The entire reaction cycle is calculated for the new smaller model (about 185–190 atoms), and two selected arcs of the wheel are chosen for calculations using a larger model (about 205 atoms). We compare the structural and redox energetics and protonation calculations with available experimental data. The reaction cycle map that we have built is positioned for further improvement and testing against experiment.



## INTRODUCTION

The question of how to effectively activate O<sub>2</sub> for reaction is of great interest in biochemistry and organic and inorganic chemistry (including materials science) because the products and byproducts of O<sub>2</sub> reactions can be variable and also because O<sub>2</sub> often encounters kinetic barriers to the reaction, “the O<sub>2</sub> overpotential”. Further, coupled electron–proton transfers, both sequential and concerted, are a major theme in the reaction chemistry of redox-active systems, including many biologically important metalloenzymes. Proton-pumping redox enzymes are functionally essential for energy storage but diverse in their mechanisms and structures, comparing cytochrome *c* oxidases (CcOs, complex IV) to cytochrome *b*<sub>c</sub> centers (complex III), for example.

Two main classes of mechanisms have been proposed for proton pumping in CcOs: (1) a direct mechanism where the chemistry of O<sub>2</sub> reduction is directly coupled to proton pumping within the O<sub>2</sub> binding dinuclear complex (DNC) containing an Fe–heme and Cu sites (Fe–a<sub>3</sub> and Cu<sub>B</sub>); (2) an indirect mechanism where conformational or electrostatic interactions with the surrounding protein, in particular with the neighboring redox donor centers in the enzyme, are required. Our current and past work has centered on potential direct mechanisms for both fundamental and practical reasons.

The driving force for proton pumping resides in the metal redox and O<sub>2</sub> binding/reduction chemistry of the DNC, so this is clearly a good place to start. By analyzing what the DNC can do with the other relevant sites as simple inputs, we want to identify the distinctive positive features as well as the potential limitations of our models. Our viewpoint is modular, which simplifies analysis where separability is valid, and reveals its limitations, where predictions prove questionable or false. Our work is an illustration of the theme that while “the map is not the territory”,<sup>1</sup> to understand the territory, it is best to build and improve the map.

Following up on our earlier work,<sup>2</sup> we explore how different metal and tyrosine redox and electronic states interact with molecular O<sub>2</sub> binding to promote proton transfer and proton pumping in the DNC of CcO. The theoretical/computational tools are spin-polarized broken-symmetry density functional theory (BS-DFT) in conjunction with continuum solvation

**Special Issue:** Insights into Spectroscopy and Reactivity from Electronic Structure Theory

**Received:** February 14, 2014

**Published:** June 24, 2014

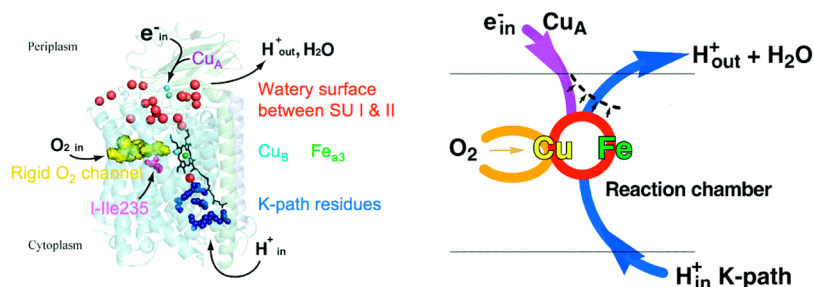
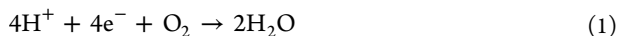


**Figure 1.** Schematic (left) of cytochrome  $ba_3$  with noted functionalities and cartoon of the same (right) showing the  $O_2$  channel inside the lipid bilayer, the reaction chamber between Cu and Fe, and the electron- and proton-transfer “pipes”. Heme-b is not shown.

dielectric modeling for the surrounding protein–solvent environment.

## BIOCHEMICAL BACKGROUND

Mitochondrial and bacterial respiration are the major sources of functional energy via adenosine triphosphate (ATP) synthesis in aerobic organisms.<sup>3–7</sup> CcOs are the terminal electron acceptors in the respiratory chain of mitochondria and many bacteria.<sup>3–5</sup> Essentially,  $O_2$  linked to the metal center is the final sink for electrons from the earlier electron-transfer complexes I–III and mobile carriers [ubiquinone (Q) and cytochrome  $c$ ]

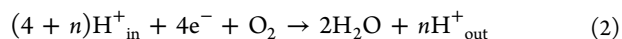


There are a number of critical functional requirements for the operation of eq 1 within the dinuclear heme iron–copper complex of CcO. Electrons and protons must be taken up at various steps of the catalytic cycle,  $O_2$  must be efficiently bound and activated for reaction without releasing oxygen-radical intermediates like superoxide anion  $O_2^{\bullet-}$  or other toxic products [for example, hydrogen peroxide ( $H_2O_2$ )], and protons must be transported to and react with metal-bound  $O_2$  and/or its subsequent intermediates. Equation 1 summarizes the relevant net chemical reaction but not the mechanism or the essential coupling to proton pumping.

Proton pumps like CcO are enzymes coupled to energy transduction machines.<sup>6,7</sup> Beyond the chemistry of eq 1, the free energy of this reaction in CcO has to be effectively utilized for proton pumping from the inside (in) to the outside (out) of the membrane against the electrochemical gradient (Figure 1). Figure 1 is a modified and annotated version of Figure 1 in ref 2 representing the structure of the bacterial B-type enzyme from *Thermus thermophilus* (Tt). Important inputs into the dinuclear Fe–Cu reaction center (DNC Cu is  $Cu_B$  and the corresponding Fe is  $Fe-a_3$ ) are shown. The dinuclear Cu–Cu center called  $Cu_A$  is shown by two small blue dots. Heme-b, which is the immediate donor of electrons to the DNC Fe–Cu center, is not shown; heme-b lies behind heme- $a_3$  in this orientation. Many spectroscopic and kinetic studies show that electrons are donated from  $Cu_A$  to heme-b Fe and then to the DNC heme- $a_3$ . Further,  $O_2$  binding is ordered compared to electron ( $e^-$ ) transfer, so that typically all four metal redox centers are  $1e^-$ -reduced before  $O_2$  binds to the DNC reaction site between  $Fe-a_3$  and  $Cu_B$ .

In standard bioenergetics language, the inside is the “n” or negative side (Figure 1, bottom, cytoplasm) and the outside is the “p” or positive side of the membrane (Figure 1, top, periplasm) corresponding to the polarity of the membrane electrochemical gradient. The detailed mechanism of proton

pumping is far from evident, but the overall reaction stoichiometry is



over a full reaction cycle. Some language is useful for bookkeeping: of the  $(4 + n)H^+_{in}$  entering the reaction chamber,  $4H^+$ , called “scalar protons”, react with  $O_2$  to produce  $2H_2O$ , while the other  $nH^+$ , called “vector protons”, are pumped across the membrane. Measurements of  $n$  have yielded values near  $n = 4$  for A-type CcOs, but lower values near  $n = 2$  have been measured for B- and C-type CcOs. (For example, extrapolating the charge-transfer measurements for the oxidative half of the reaction cycle to the entire oxidative plus reductive reaction cycle for B-type Tt  $ba_3$  yields  $n = 2.5$  approximately.<sup>8</sup>) Finding accurate experimental values for  $n$  is difficult, and significant uncertainties remain.

In common with respiratory chain complexes I and III<sup>5–7</sup> and ordered sequentially by increasing redox potentials, complex IV links  $e^-$  transfer down the electron-transport chain to proton pumping across the inner membrane of the mitochondria and, analogously, across the plasma membrane in most aerobic bacteria. The resultant proton electrochemical gradient, or proton motive force, is utilized for ATP synthesis from adenosine diphosphate (ADP) plus inorganic phosphate by complex V (ATP synthase), which also resides within the same membrane. The proton electrochemical gradient has a higher positive potential on the outside (p) of the membrane and a lower negative potential on the inside (n) of the membrane (matrix side in mitochondria). The proton leak “downhill” across the membrane is largely funneled through the ATP synthase active site to generate ATP from ADP+Pi. As expected from energy conservation, continued proton pumping is required to maintain the membrane potential against the leak and to provide the driving force for ATP synthesis. Alternatively, if the electrochemical gradient is depleted, proton pumping is required to restore the gradient. The electrochemical potential is the sum of an electrical potential (voltage) difference,  $\Delta\Psi$ , and a pH difference,  $\Delta pH$ , across the membrane

$$\Delta\mu_{H^+} = \Delta\Psi - 2.3RT(\Delta pH)/F \quad (3)$$

where  $F$  is the Faraday constant.

While the reaction inputs and outputs of the respiratory complexes are understood in broad stroke, in no case is the actual coupled electron redox/proton pumping mechanism understood in even reasonable detail. Many features are known from spectroscopy and kinetics about the chemical mechanism of  $O_2$  reduction and subsequent mechanistic steps of the reaction cycle, but there is no current resolution about whether

or how proton pumping is directly coupled to the chemistry of  $O_2$  reduction at the Fe–Cu DNC or indirectly coupled through conformational or electrostatic changes in the surrounding protein, particularly involving the nearby redox centers (the  $Cu_A$  homodinuclear and mononuclear Fe-heme donor centers).<sup>9–11</sup> It is possible that the different enzyme classes A1 versus B could have significant differences in their mechanisms (see the later discussion), including whether a direct or indirect mechanism (or some mixture) applies.

X-ray crystallographic structures are now available for mitochondrial [bovine heart (*Mt*)] and several bacterial CcOs, including *Paracoccus denitrificans* (*Pd*), *Rhodobacter sphaeroides* (*Rs*; all A1 type), and *T. thermophilus* (*Tt*; B type).<sup>3,12–16</sup> The *Mt* structure is by far the most complex, with 13 subunits (3 encoded by mitochondria and 10 by the nucleus). However, the three mitochondrial subunits (I–III) of *Mt* closely resemble the corresponding subunits in the bacterial enzymes *Pd* and *Rs*, and all are of class  $aa_3$ . The *Tt* enzyme is of a different class (namely,  $ba_3$ ) but still has many similarities in sequence, structure, and mechanism to the other CcOs. The bacterial enzymes are easier to work with than the more complex *Mt* protein and have, therefore, been subjected to studies using systematic mutagenesis of different sites. Our main focus will be on analysis of the *Tt* enzyme, for which Fee, Stout, and co-workers have obtained high-resolution X-ray structures, including several different mutants, and measured kinetic spectroscopic parameters of many intermediates over the redox and catalytic cycle.<sup>12,13,17–19</sup> Kinetic analysis is enhanced in  $ba_3$ -type enzymes including *Tt* because the absorption spectrum of heme-b is well-separated from that of heme- $a_3$  in contrast to  $aa_3$  (A type) enzymes, where the heme- $a$  and - $a_3$  bands overlap. Also, importantly, the *Tt* enzyme has a single input path ( $K_B$  path) for protons into the dinuclear Fe–Cu center, which simplifies analysis of the proton pathways compared to two paths for A1-type enzymes. While the  $K_B$  path occupies a structurally analogous region compared to the  $K$  path in A1 enzymes, the  $K_B$  path does not contain lysine, in contrast to the  $K$  path in A1.

The biological  $e^-$ -transfer sequence proceeds<sup>17</sup> in one electron ( $1e^-$ ) steps from cytochrome  $c$  to the dinuclear mixed-valence  $Cu_A$  site in subunit II (having a  $2Cu^{1.5+}$  center in the oxidized state and  $2Cu^+$  in the reduced), to a mononuclear Fe-heme redox center in subunit I (which in *Tt* is heme-b but in *Pd*, *Rs*, and *Mt* is heme-a), and finally to the dinuclear heme- $a_3$ –Fe– $Cu_B$  reaction center, which is also in subunit I and is where  $O_2$  binds. The proton entry pathway is simpler in the *Tt*  $ba_3$  enzyme, having a single entry pathway called the “ $K_B$  path”, compared to two potential entry pathways, called the “ $K$  and  $D$  paths”, in the class  $aa_3$  enzymes.  $O_2$  enters via a well-defined hydrophobic pocket near the dinuclear Fe- $a_3$ – $Cu_B$  site. Figure 1 (left) shows an overall structural model of CcO from *Tt* with the inputs and outputs superposed, and Figure 1 (right) is a cartoon of the reaction chamber with reactants and products. In *Tt*  $ba_3$ , the subunit I residue Ile235 is present (see Figure 1) in place of a glutamate residue present in A1-type enzymes, so that the second proton-transfer pathway (the  $D$  or  $Q$  proton-transfer pathways seen in A1-type enzymes) is absent in B-type enzymes. This also eliminates the corresponding path to the “proton loading site” as proposed in A-type enzymes. The significant implication is that the path into the DNC is common to both the scalar and vector protons. Any subsequent bifurcation of proton flow between the scalar and vector pathways occurs at or after the entry point into the DNC.

Mitochondrial CcOs play an essential role in human health. Adequate ATP supplies are necessary for all important metabolic cellular functions.<sup>4</sup> Also, disruptions in  $O_2$  binding and electron- or proton-transfer reactions at CcO can lead to an excess of reactive oxygen species including hydroxyl and superoxide radicals. These oxygen species can arise directly at CcO or can be induced earlier in the electron-transport chain, for example at complexes I and III, because of a blockage in electron or proton transport at CcO. Finally, disruptions in the normal proton-transport pathways may also have damaging effects on the membrane potential and acidity in the matrix or periplasmic space. Understanding the structures, mechanisms, and functions of mitochondrial CcO is therefore important for better analysis of genetic and metabolic diseases and cancer and is also relevant to pathologies in aging.<sup>3–7,20,21</sup> Mitochondrial DNA is intrinsically subject to elevated mutation frequency possibly because of its proximity to leaky electron-transport chains that produce reactive oxygen species. The close functional and mechanistic relationship between mitochondrial CcO and various bacterial CcOs allows for the development of an overview of the catalytic proton-pumping cycle, while variations in the structures and energetics/kinetics can provide insight into the interactions between different redox centers and proton sources.

The A-type enzymes in *Pd* and *Rs* reside in  $\alpha$  proteobacteria, some of which were probably ancestors of eukaryotic mitochondria. B-type enzymes, while simpler in some ways, also show significant variations in different species/genera. Further, mutagenesis studies in bacteria provide a good way of examining blockage and inhibition of proton and electron transfer and  $O_2$  binding. There have also been very significant accomplishments in making synthetic analogues of the DNC, and testing the reaction, physical, and spectroscopic properties of these systems.<sup>22–24</sup>

## ■ ELECTRON FLOW WITHIN CCO

Electron flow in both A1- and B-type CcOs has been studied extensively. Electrons transfer from cytochrome  $c$  to  $Cu_A$ , then on to heme- $a$  (or heme- $b$  in A1 and B types, respectively), and from there to Fe- $a_3$ – $Cu_B$ .<sup>8,25</sup> After  $O_2$  binding to the DNC, a number of oxygen-derived intermediates are formed. A good deal is known about the timing of  $O_2$  binding and  $e^-$  transfer by binding CO to heme- $a_3$  and then introducing  $O_2$ , followed by photolyzing the CO in the fully reduced or half-reduced (mixed-valent) forms of the bovine and related bacterial enzymes. However, CO photolysis experiments have some difficulties, as discussed below.

## ■ REACTION CYCLE OF THE DNC IN CCO

Because of their considerable structural and functional similarities, A- and B-type enzymes probably have a common mechanism of  $O_2$  reduction. Using optical spectroscopy to monitor transient kinetics, Siletsky et al.<sup>8</sup> and Szundi et al.<sup>26</sup> observed four intermediates for reduction and  $O_2$  binding and reactions in *Tt* cytochrome  $ba_3$  at the DNC, as shown in Figure 2. To obtain proper timings for kinetics, the reaction of the fully reduced enzyme is started by photolysis of the reduced Fe- $a_3$ –CO adduct of the enzyme in the presence of  $O_2$ , and then changes in a wide array of properties are followed from the nanosecond to second time scale. Here the fully reduced enzyme includes the fully reduced state (**R**) of the DNC and the reduced states of heme- $b$  and  $Cu_A$ .



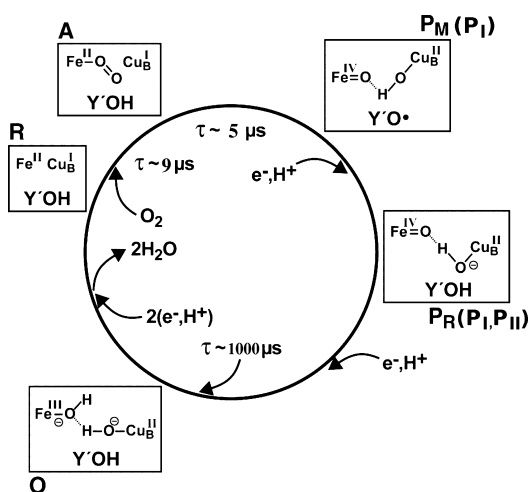


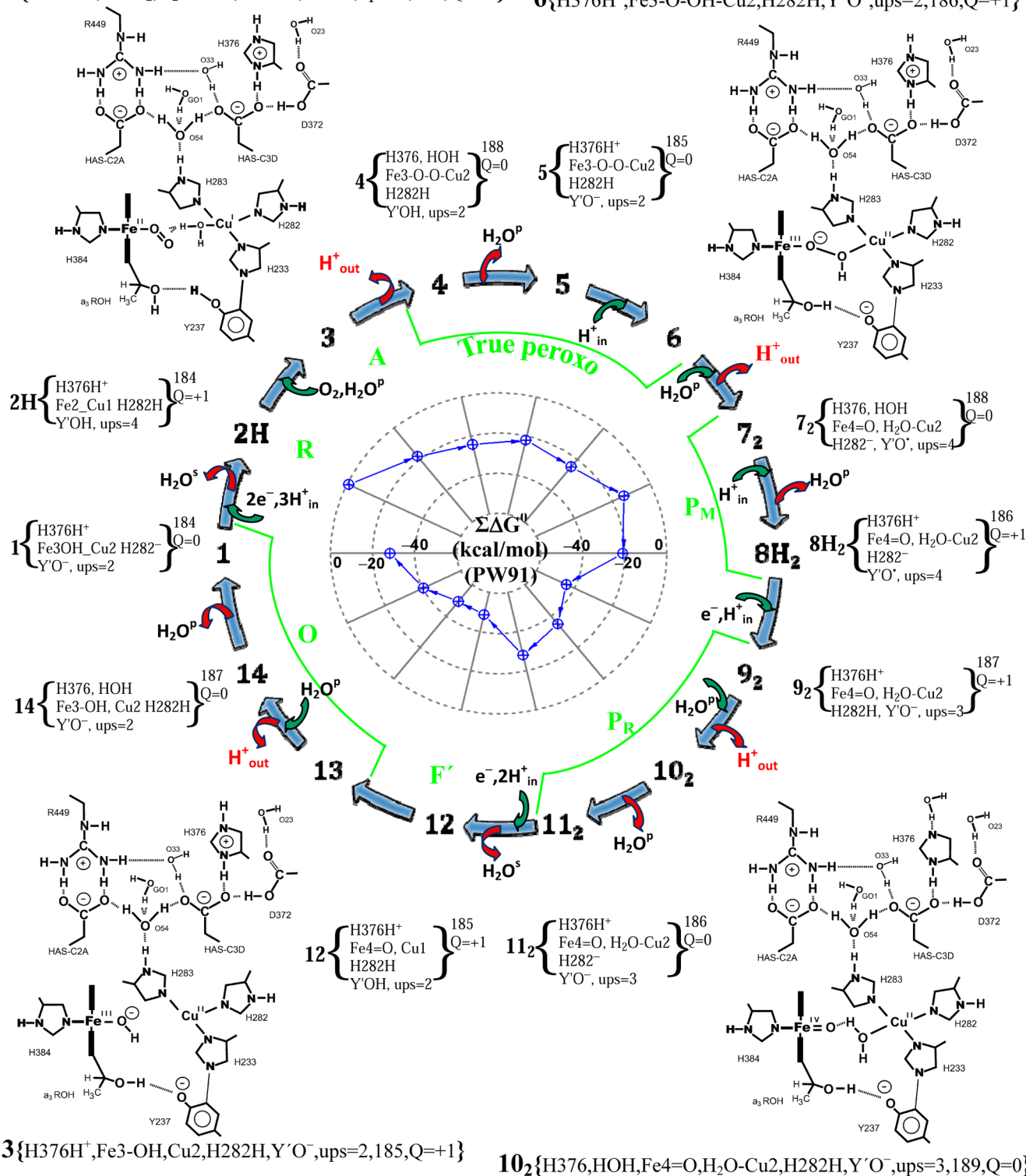
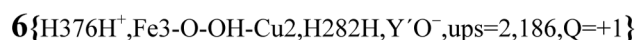
**Figure 2.** Catalytic “wheel” of cytochrome  $ba_3$  focusing on the DNC. Concentration of  $O_2$  for  $R \rightarrow A$  is  $90 \mu M$  for  $\tau \approx 9 \mu s$ , from Szundi et al.<sup>26</sup>

Compounds **A**, **P<sub>I</sub>** (where **P<sub>I</sub>** is likely composed of both **P<sub>M</sub>** and **P<sub>R</sub>**), and **O** in *Tt*  $ba_3$  are similar to their analogues in A1-type enzymes. More broadly, the optical absorption difference spectra of heme- $a_3$  do not clearly report on the oxidation state (or related chemical/electronic features) of either  $Cu_B$  or the unusual tyrosine called  $Y'OH$ . Recently, Szundi et al.<sup>26</sup> found that the early oxidative steps of the reaction become unreliable with the CO photodissociation method because CO can then bind to  $Cu_B$ , and this inhibits  $O_2$  binding to Fe- $a_3$  and  $Cu_B$ . Instead of using CO bound to the reduced state **R**, they instead utilized a photolabile  $O_2$  carrier complex to deliver  $O_2$  to the DNC. The kinetics are then clarified by examining different concentrations of  $O_2$  delivered to the DNC. Lifetimes ( $\tau$  = inverse of rate constants  $r$ ) from this study are assembled in Figure 2. These lifetimes differ from those we previously presented based on Siletsky's kinetic studies.<sup>2</sup> Starting from state **R**,  $O_2$  binding occurs very rapidly (even at the low effective  $[O_2] = 90 \mu M$ ) and so does the following formation of ferryl-oxo states, spectroscopic state **P<sub>I</sub>**. State **P<sub>I</sub>** is a combination of electronic/protonation states **P<sub>M</sub>** and **P<sub>R</sub>**, and because the heme-b Fe is also reduced, the very fast  $e^-$  transfer to reduce the tyrosine radical is not detectable in these experiments. (The state **P<sub>M</sub>** is detected in separate experiments, where the  $O_2$  reaction is started from the “mixed-valence state”, with the DNC being in state **R**, while the heme-b and  $Cu_A$  sites are oxidized. Then the cycle stops at **P<sub>M</sub>** because of a lack of reducing electrons.) The cycle depicted in Figure 2 omits the next spectroscopically observed intermediate, **P<sub>IV</sub>**, which corresponds to the timing for  $e^-$  transfer from reduced  $Cu_A$  to oxidized heme-b Fe, which was the redox center oxidized in the **P<sub>M</sub>**  $\rightarrow$  **P<sub>R</sub>** transition. After the heme-b Fe is reduced, it is ready to deliver the final electron in the transition **P<sub>R</sub>**  $\rightarrow$  **O**, which is comparatively slow. The reaction cycle experiments of Szundi et al. end with state **O**.<sup>26</sup> Recent pulse radiolysis experiments<sup>27</sup> have shown a comparatively slow  $1e^-$ -transfer rate from state **O** (reducing agent heme-b Fe) to heme- $a_3$  Fe (III  $\rightarrow$  II), lifetime  $\tau = 4800 \mu s$ , compared to faster  $e^-$  transfer from  $Cu_A$  to heme-b,  $\tau = 260 \mu s$  in *Tt*  $ba_3$ . Therefore, both **P<sub>R</sub>**  $\rightarrow$  **O** and **O**  $\rightarrow$  **R** have comparatively slow  $e^-$  transfers. We have argued in our published work<sup>2</sup> that  $e^-$  transfer from heme-b (reduced) to the DNC may be determined by the nature of the oxidant center present on heme- $a_3$ , which is likely to involve

both reorganization energy terms and the driving force (redox potentials) for different reaction steps.

For future reference, we comment briefly on the issue of the electrochemical potential (load versus no or low load) in kinetic studies and proton-pumping experiments.<sup>7</sup> When experiments are conducted in detergents and/or buffers, there is no net directionality (vectorial character) to the orientation of the CcO proteins in the media, and so there is no net electrochemical potential. For kinetic studies, these types of conditions are often used,<sup>17,26,27</sup> and they lead to faster kinetics than those in the presence of an electrochemical potential (experiments under load). Even X-ray crystallographic experiments done in the lipidic cubic phase have no net directionality (see Tiefenbrunn et al.<sup>19</sup>) because the individual CcO proteins are aligned antiparallel in the lipidic cubic phase. By contrast, experiments designed to measure the proton-pumping stoichiometry or net charge ( $q$ ;  $e^-, H^+$ ) transfer across the membrane (usually vesicle experiments) are set up so that the CcO proteins have specific directional alignment with respect to the inside versus outside of the vesicles. Proton-pumping stoichiometry (vector protons) is typically determined by running a full or partial cycle and collapsing the electrical potential difference across the vesicle using an ionophore, which does not conduct protons but does conduct some other charged particles. (For example, valinomycin allows counter-transport of  $K^+$  ions when protons are pumped in the CcO reaction cycle.<sup>7,28</sup>) In that case,  $\Delta pH$  is measured in the corresponding partial cycle. To measure full charge transfer, corresponding to electrons, scalar protons, and vector protons driven against the existing gradient, measurements of the electrical potential change over a partial cycle are obtained. Both for proton pumping and net charge transfer, the standing electrochemical potential (and its electrical component) is typically much less than that under actual physiological conditions. (Usually, the electrical term dominates eq 3 under physiological conditions in mitochondria and analogously in aerobic bacteria.<sup>7</sup> So, in practice, most proton-pumping and charge-stoichiometry experiments are under low load.

Our DFT calculations for the reaction cycle are performed under idealized pH gradient conditions, where we assume that each pumping of a vector proton across the DNC corresponds to transfer from a neutral pH = 7 cytoplasm (n side) to an acidic pH = 3 periplasm (p side), and there is no electrical potential gradient, as in the vesicle experiments with an ionophore described above. This makes bookkeeping for the cost of proton pumping easy because only the vector protons have a cost, which is accounted for as the proton exits from the DNC. By contrast, a standing electrical potential across the membrane will lead to a pump cost for the vector protons and to a cost for charge transfer for the electrons and scalar protons because these combine in the reaction chamber of the DNC. The energy accounting here is more complex, and we will defer it to future work. (For a simple analysis, see Siletsky et al.<sup>8</sup>) However, there is one general observation that is very useful. If the same energy cost over an entire cycle (say for pumping four vector protons from pH = 7 to 3) is instead distributed over both the vector proton transfers and the scalar proton plus electron transfers as occurs for an electrical potential difference, rather than a pH difference, the charge-transfer cost across the DNC over individual steps is considerably less (roughly  $1/2$  or less because there are  $q = 8$  charges transported across the membrane versus  $n = 4$  vector protons).



## ■ OBJECTIVES OF THE THEORETICAL/COMPUTATIONAL CYCLE

known features of the experimental reaction scheme but goes well beyond what is presently established. Very recently, we have further refined the DFT model by examining alternative tautomeric and protonation states.

We emphasize some important general points starting from Figure 2.<sup>8,29</sup> **(1) Electron and Proton Delivery.** The points of electron entry into the cycle as well as O<sub>2</sub> binding are well

established, but only four protons are accounted for within this scheme. These are the scalar protons as in eq 1, and the vector protons are not included (see eq 2). On the basis of eq 2, the optimal proton-pumping ratio is  $4\text{H}^+/4\text{e}^-$ , equivalent to  $1\text{H}^+/1\text{e}^-$ . Typically, experimental proton-pumping ratios are near 1, but early published measurements with  $\text{ba}_3$  yielded values of about 0.4–0.5. In any event, a pumping ratio of 1 requires a proton uptake ratio for  $\text{H}^+_{\text{in}}/1\text{e}^-$  of  $(4 + n)/4 = 2$ . Any uptake ratio greater than 1 requires special chemistry. Moreover, under physiological conditions (and in some experimental setups), the pumped protons must be moved against the electrochemical gradient at a cost in  $\Delta G^\circ$ , using the chemical driving force available from the redox/protonation reactions with  $\text{O}_2$ . (2) **Important Chemical Intermediates.** There are critical and distinctive chemical questions raised by the catalytic reaction cycle and the structure/composition of the DNC. (2a) At least one Fe–Cu bridging peroxo intermediate is likely to form subsequent to the initial oxy complex (A), which has been identified, but the peroxo intermediate(s) has not been spectroscopically identified. The peroxo complex is likely to be very short-lived<sup>26</sup> but is clearly essential to the energetics of O–O bond cleavage and for avoidance of a substantial overpotential. Both the energetics and properties of these intermediates are of great interest and are connected to binding modes and protonation states. (2b) There is a unique tyrosine (Y'OH in Figure 2) that is formed from a covalent bond between the tyrosine phenol and a histidine imidazole ring (residues Y237 and H233 in *Tt*  $\text{ba}_3$ ). Further, H233 is coordinated to  $\text{Cu}_\text{B}$ . What are the roles of this unusual linkage in the catalytic cycle? (3) **Proton Pumping by the DNC.** What is the physical mechanism connecting the redox and chemical bonding cycle to the proton pumping? The lack of mobile proton carriers within CcO precludes a “redox loop” mechanism, but CcO pumps protons, nonetheless. We have already proposed a proton exit channel into the watery surface between subunits I and II (see Figures 1 and 3). Specifically, this involves deprotonation of H376 (from the positive imidazolium form). As an alternative, deprotonation may instead involve a nearby bound water (probably a hydronium ion), which also looks reasonable. Our current working hypothesis is that the DNC complex itself and the  $\text{K}_\text{B}$  path conducting protons into the DNC are the major factors driving proton pumping. We also think that the redox potentials and timing of  $\text{e}^-$  transfer from heme-b Fe to the DNC play a role, as will be described later.

A combination of electrostatic and large-scale DFT calculations with associated energy analysis has been used to examine the proton-pumping mechanism in class A1 ( $\text{aa}_3$ -type) enzymes.<sup>11,30,31</sup> In a number of papers, Blomberg and Siegbahn<sup>32–34</sup> have proposed that  $1\text{e}^-$  transfer from the  $\text{Cu}_\text{A}$  center to the mononuclear heme-a drives protonation at a pump-loading site (PLS) close to a propionate in heme- $\text{a}_3$ , as well as protonation of the glutamate (Glu286 in bacterial *Rs* and a homologous glutamate in mitochondria). Both protons originate from the D proton channel. The Glu286 proton then activates proton exit from the PLS after  $1\text{e}^-$  transfer from heme-a to the DNC Fe site in heme- $\text{a}_3$ , with a coupled “chemical” proton transfer close to the reduced  $\text{Fe-a}_3^{2+}$  site (the  $1\text{e}^-$ -transfer step modeled is  $\text{O} \rightarrow \text{E}$ , the first  $1\text{e}^-$  transfer in the  $\text{O} \rightarrow \text{R}$   $2\text{e}^-$  reduction). The chemical proton transfer is also modeled as originating from the D channel. Presumably, at other steps of the catalytic reduction  $\text{O}_2$  binding reaction cycle, some “chemical” protons originate from the K channel. In any

event, in class B ( $\text{ba}_3$ -type) enzymes, there is no D-type proton-transfer pathway, and in *Tt*  $\text{ba}_3$ , there is an isoleucine (Ile235) in a position homologous to Glu286 (see Figure 3 in ref 35). Nonetheless,  $\text{ba}_3$  enzymes do pump protons, although probably at lower efficiency than  $\text{aa}_3$ .<sup>8</sup> (4) **Proton Entry and Flow.** Therefore, we will focus here on the catalytic reaction cycle, including proton flow into the DNC from the  $\text{K}_\text{B}$  path and particularly within the DNC itself. The vector and scalar protons almost certainly take different paths through the DNC. The currently available high-resolution X-ray structures of *Tt* cytochrome  $\text{ba}_3$ <sup>35,36</sup> from Fee, Stout and collaborators<sup>19</sup> show a much richer array of waters bound to the DNC than that seen in earlier X-ray structures at lower resolution.

## ■ MODELS AND METHODS: CATALYTIC WHEEL

(a) In our earlier paper (2008),<sup>2</sup> we constructed the entire catalytic reaction “wheel” for the cytochrome  $\text{ba}_3$  DNC, employing large-scale DFT calculations. (b) On the basis of subsequent work, we have found an improved energy path by modifying the sequence of proton uptake and proton-transfer events and examining alternative proton tautomeric states. These two sets of models each contain 183–189 atoms and are called S1 and S2, for the original and for the newer model encompassing different tautomers for several states. Both models are based on the Hunsicker-Wang and Fee X-ray structure of  $\text{ba}_3$ .<sup>12</sup> Both of the smaller models are computed with a Perdew–Wang (PW91) exchange-correlation potential for geometry optimization in a dielectric medium with dielectric constant  $\epsilon = 18.5$  for the surrounding environment. Then single-point PW91 and B3LYP\* calculations are compared over the reaction path. (c) For selected parts of the catalytic reaction path, we have now introduced a larger model (L), incorporating additional waters and residues and with greater flexibility in the electronic states described. The larger model is built based on the high-resolution (1.8 Å) X-ray structure of Tiefenbrunn et al.<sup>19</sup> in the lipidic cubic phase, which has a higher density of water in the protein interior. As discussed in a recent paper,<sup>37</sup> the observed X-ray structure contains a bound dioxygen species that is probably hydroperoxide. As in the Hunsicker-Wang and Fee (2.3 Å resolution) X-ray structure,<sup>12</sup> the DNC in the protein is probably radiolytically reduced, but within DFT, we can control the oxidation state and the types of bound ligands that are introduced in the calculations. The model L calculations utilized an OLYP exchange-correlation potential. Because of the increased cluster size, we found that the calculations could be performed with fewer geometric constraints. In particular, only the link atoms at the outside boundary of the quantum cluster were constrained to their positions in the Tiefenbrunn X-ray structure, as specified in ref. 37. The dielectric model is the same as models S1 and S2, and all use the COSMO solvation model.<sup>38–41</sup> All calculations use the ADF codes.<sup>42,43</sup>

## ■ CATALYTIC REACTION CYCLE RESULTS AND DISCUSSION

**Small Models.** The catalytic wheel diagram for the DNC from our new model S2 is presented in Figure 3. From geometry optimization and energy evaluation of 30 different tautomeric/net protonation states (defined as model  $\text{S}_{\text{all}}$ ) for the 14-step cycle, we have selected 14 states in model S2. Compared to model S1,<sup>2</sup> if a different tautomer is chosen in S2, this is indicated by a subscript on the state number, for



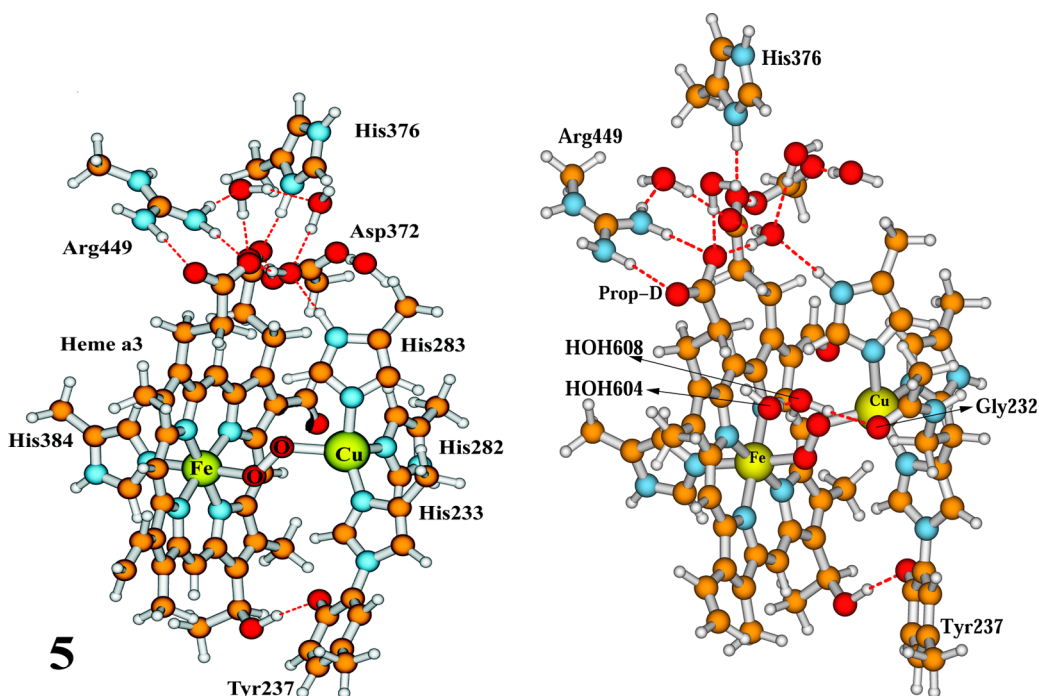


**Figure 4.** Active site structure of compound **5** of  $ba_3$ . Left: smaller model used in the 2008 calculations.<sup>2</sup> Right: larger model used in recent calculations,<sup>37</sup> which is taken from the DNC of the high-resolution (1.8 Å) X-ray crystal structures (PDB entry: 3S8G) of  $ba_3$  CcO from *Tt*.<sup>19</sup> For ease of visualization, these two models are not on the same scale.

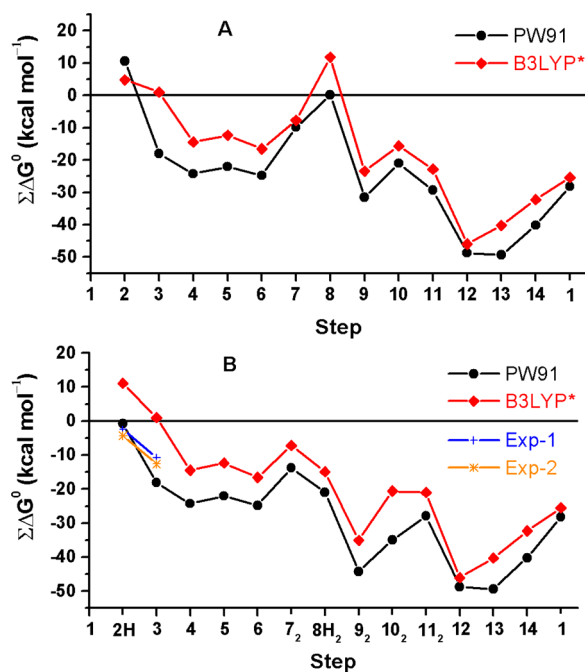
example,  $7_2$  versus  $7$ . Where a proton has been added, this is indicated by an H, so; for example,  $2H$  compared to  $2$  and  $8H_2$  compared to  $8$  indicate both a tautomeric shift and an additional proton added.

Figure 3 shows a detailed map of the catalytic reaction cycle for model S2. See also the related cycle in ref 2. We have augmented the figure by labeling intermediates **O**, **R**, **A**, **P<sub>M</sub>**, and **P<sub>R</sub>**, which have all been observed spectroscopically. All of these intermediates have approximate counterparts in Figure 2, and the theoretical scheme is supported by detailed DFT calculations. Most of the spectroscopic intermediates correspond to more than one detailed intermediate in the 14-state reaction cycle. For example, states **13**, **14**, and **1** correspond to experimental intermediate **O**; all of these states are  $Fe^{III}-Cu^{II}$  species, but they differ with respect to protonation state(s) or  $H_2O$  binding. In addition, our catalytic wheel includes “true peroxo” states not seen spectroscopically, which are testable by energetic calculations and potentially by spectroscopic measurements when these (or related states) are isolated. Structures **3**, **6**, **10**, and **13** are detailed 2D maps of the dinuclear  $Fe-a_3-Cu_B$  center, while the other states are represented by simple chemical formulas. A full 3D picture of the  $Fe^{3+}-(O-O)^{2-}-Cu^{2+}$  bridging peroxo state, intermediate **5**, is shown in Figure 4. By comparison with Figure 3, the coordination, covalent, and hydrogen bonds are quite clear in the 2D maps, but the 3D links are distorted; for example, the heme propionate side chains are attached to the Fe-heme edge.

The new 14-step cycle differs from the previous one<sup>2</sup> in (1) having protons enter the reaction path earlier at two steps,  $1 \rightarrow 2H$  and  $7 \rightarrow 8H_2$ , (2) retaining water in state  $11_2$  compared to state **11**, and (3) utilizing different proton tautomers, for all of the states where there are subscripts in Figure 3. (The original tautomers from model S1 are not subscripted.) By convention, tautomers from model S1 are each tautomer 1; for example,  $6 = 6_1$ . In constructing the intermediates in Figure 3, we mainly

stayed with the lowest-energy tautomers. The one exception is state **6**, which is critical to the peroxide cleavage reaction. In our model S2, this is  $6 \text{ kcal mol}^{-1}$  higher (in PW91) than the lowest tautomer,  $6_2$ , where the special tyrosine (Y237) is protonated in place of the peroxide. As we will show later, both tautomers  $6_2$  and **6** are energetically feasible along the reaction path. The outcome of replacing our original reaction path (model S1) with one constructed from the lowest-energy tautomers (also alternate protonation states) is shown in Figure 5, comparing parts A and B. The effect is striking. These changes to the previous mechanism result in a substantially “smoother” catalytic cycle. The largest positive free-energy difference  $\Delta G^\circ$ , accounting for successive uphill steps, is lowered to about  $20 \text{ kcal mol}^{-1}$  for PW91 in model S2 ( $31 \text{ kcal mol}^{-1}$  in B3LYP\*), while in the reaction pathway of model S1 for both PW91 and B3LYP\*, this value is close to  $30 \text{ kcal mol}^{-1}$ . It is easy to see that both exchange-correlation potentials run in a similar manner for energies over the reaction cycle and that Figure 5B shows a more reasonable cycle for both PW91 and B3LYP\*. The  $\Delta G^\circ$  values for individual steps are considerably less in all cases (about  $15 \text{ kcal mol}^{-1}$  maximum). Accounting for transition states using standard transition state theory will also give barriers larger than those from  $\Delta G^\circ$  steps between intermediates, while concerted processes and/or proton tunneling may well lower the effective barriers.

One protonation step that promotes the catalytic cycle is to add one additional proton to  $Y'O^-$  in the transition  $1 \rightarrow 2$  to make the state  $2H$ , so that the added proton transfer from the  $K_B$  path to Y237 is effectively concerted with  $2e^-$  reduction of  $Fe^{3+}-Cu^{2+}$  to give  $Fe^{2+}-Cu^+$ . Our computed redox potentials for  $1 \rightarrow 2H$  are  $0.24 \text{ V}$  for PW91 and  $-0.02 \text{ V}$  for B3LYP\*, versus  $0.275 \text{ V}$  (experimental average<sup>44,46</sup> for  $Cu^{II} \rightarrow Cu^I$ ,  $+0.34 \text{ V}$ , and  $Fe^{III} \rightarrow Fe^{II}$ ,  $+0.21 \text{ V}$ , for mitochondria) or  $0.314 \text{ V}$  using the experimental redox potential for  $Fe^{III} \rightarrow Fe^{II}$  for *Tt*  $ba_3$ .<sup>45</sup> The corresponding error in  $\Delta G^\circ$  is about  $1.6\text{--}3.1 \text{ kcal}$



**Figure 5.** Plots of  $\Sigma\Delta G^\circ$  (kcal mol<sup>-1</sup>) along the trajectory from 1 to 14. The top panel (A) is from the 2008 mechanism (from Table 4 for energies);<sup>2</sup> the bottom panel (B) represents new work presented here. Solid black circles represent energies obtained from PW91 calculations, while reddish diamonds represent energies obtained from B3LYP\* calculations. The experimental energies from 1  $\rightarrow$  2 and 2  $\rightarrow$  3 are obtained from refs 26 and 44–46.

mol<sup>-1</sup> for PW91 and about 13.5–15.5 kcal mol<sup>-1</sup> for B3LYP\*. In contrast to state 1  $\rightarrow$  2H (O  $\rightarrow$  R), the calculated O<sub>2</sub> binding affinity (for standard state [O<sub>2</sub>] (aqueous) = 1 M) is much poorer for PW91 than B3LYP\*,  $\Delta G^\circ = -17$  and  $-10$  kcal mol<sup>-1</sup>, respectively, versus  $-8.3$  kcal mol<sup>-1</sup> experimental for *Tt* ba<sub>3</sub> from the reaction kinetics study of Szundi et al.<sup>26</sup> (see also Figure 2; state 2H  $\rightarrow$  3, R  $\rightarrow$  A). These few available experimental values are plotted in Figure 5B. Experimental kinetics work of Hallen and Nilsson<sup>47</sup> shows that there is no proton uptake when O<sub>2</sub> binds (noting that these are experiments in mitochondria), which is consistent with state 2H  $\rightarrow$  3 (Figure 5B) rather than 2  $\rightarrow$  3 (Figure 5A) and is correctly represented in PW91 but not B3LYP\*.

The K<sub>B</sub> path into the DNC based on Tiefenbrunn, Fee, and Stout's high-resolution X-ray structure<sup>19</sup> is depicted in Figure 6. All residue side chains are constructed based on the X-ray density map, except for one added water (center purple), which completes the hydrogen-bonding network from Glu15(II) (from subunit II) to Y237 of the DNC and involves a<sub>3</sub>-ROH from the lower heme edge. The orientation of Figure 6 is 180° rotated about the vertical axis with respect to Figures 3 and 4 so that the Cu site is toward the left (above Y237) and Fe is toward the right. Figure 6 shows the structure of the K<sub>B</sub> path for protons into the DNC in *Tt* ba<sub>3</sub>. The Glu15(II) anion is positioned to accept a proton from the solution (n side) and return to a hydrogen-bond alignment. Then a proton can be readily transferred via a concerted Grotthuss-type process<sup>48</sup> (in common language, "a bucket brigade mechanism") to Y237. Finally, the Glu15(II) anion picks up another proton. Usually we expect that the destination for the proton is Y237<sup>-</sup>, but the geranylgeranyl a<sub>3</sub>-ROH group provides an additional entry point into the complex where an alternative pathway is needed.

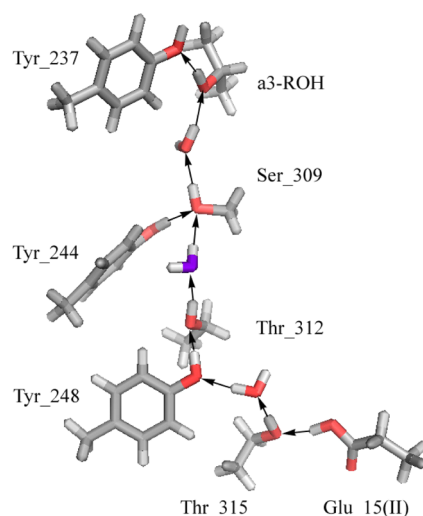


**Figure 6.** Structure of the K path in cytochrome ba<sub>3</sub> as deduced from a combination of structural and mutational analyses. The top two residues are actually part of the active site structure per se. Both Glu15(II) and Y237 are protonated. This figure is taken from Figure 2 of ref 35. Reprinted with permission from ref 35. Copyright 2009 National Academy of Sciences.

To examine the physical/chemical forces that drive proton pumping across the DNC, we now look at the path from state 4 to 5 and include an additional tautomer S<sub>2</sub>. Compared to state 4, state S<sub>2</sub> has a proton shifted from H282 to H376 to form a state with H376H<sup>+</sup>, H282<sup>-</sup>, and YOH. The proton-shift distance is much smaller than that directly from state 4 to 5, and the predicted energy cost is small (7 kcal mol<sup>-1</sup> for state 4  $\rightarrow$  S<sub>2</sub>, followed by  $-5$  kcal mol<sup>-1</sup> for S<sub>2</sub>  $\rightarrow$  5, in place of 2 kcal mol<sup>-1</sup> for state 4  $\rightarrow$  5 in PW91; in B3LYP\*, both energy differences are near 2 kcal mol<sup>-1</sup>). State 5 is then generated by shifting a proton in S<sub>2</sub> from neutral Y237 (YOH) to H282<sup>-</sup> to form YO<sup>-</sup>, H282H. In Figure 7, the structures of these states are presented with the dipole moment vectors superimposed in red and the magnitudes labeled [ $\mu$  in Debye (D) units]. Because dipole moment vectors are oriented from negative to positive, it is clearly seen that the proton shifts strongly reorient the very large dipole moment vector from 4  $\rightarrow$  S<sub>2</sub>  $\rightarrow$  5, so that state 4 is almost oppositely aligned to state 5. The corresponding electrostatic potential becomes more positive in the vicinity of H376H<sup>+</sup>, or alternatively in the nearby water cluster (top of Figures 3 and 4). The following proton entering via the K<sub>B</sub> path ends in state 6 (see Figure 3), but the proton entry state is tautomer 6<sub>2</sub> (Fe<sup>III</sup>-O-O<sup>2-</sup>-Cu<sup>II</sup>, YOH). State 6<sub>2</sub> is 6 kcal mol<sup>-1</sup> below state 6 in PW91, so the path 5  $\rightarrow$  6<sub>2</sub>  $\rightarrow$  6 has energy differences ( $-8.7$  and  $+6$  kcal mol<sup>-1</sup>). After proton entry in state 6<sub>2</sub>, the proton shift to form the hydroperoxide in state 6 produces an increase in the dipole moment magnitude of about 13 D, in a direction similar to that in state 5, again enhancing the electrostatic potential near H376. As shown in Figures 3 and 5B, the energy difference 6  $\rightarrow$  7<sub>2</sub> is only mildly endergonic (11 kcal mol<sup>-1</sup> in PW91; pumping against an assumed proton gradient from the pH = 7 n side to the pH = 3 p side, equivalent to 5.5 kcal mol<sup>-1</sup>).

As expected on physical grounds, reducing Cu<sup>II</sup>  $\rightarrow$  Cu<sup>I</sup> in the preceding step 1  $\rightarrow$  2 increases the proton affinity of the covalently linked Y327-H233 pair bonded to Cu ( $\Delta G^\circ = -11.4$  kcal mol<sup>-1</sup> for PW91 for 2  $\rightarrow$  2H, so  $\Delta G^\circ$  is lowered for 14  $\rightarrow$  2H to 11.1 kcal mol<sup>-1</sup> compared to that for 14  $\rightarrow$  2,



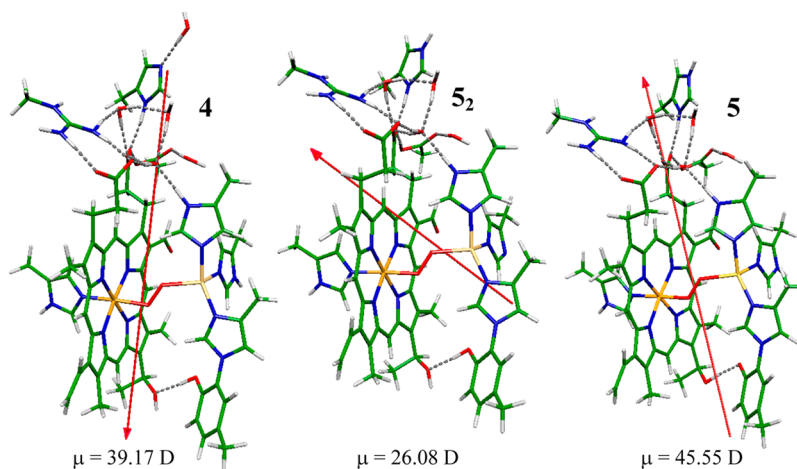


**Figure 7.** Dipole moments of intermediates 4, 5<sub>2</sub>, and 5. These three structures are overall neutral.

+22.5 kcal mol<sup>-1</sup>). This is also consistent with the experimental observation that O<sub>2</sub> binding is not pH-dependent because that proton enters earlier at state 2H.

After O<sub>2</sub> binding and formation of a peroxo-type bridge and higher Fe and Cu oxidation states, (Fe<sup>3+</sup>, Fe<sup>4+</sup>) and Cu<sup>2+</sup>, we expect that Cu<sup>2+</sup> would acidify Y237–H233 (i.e., the Y'OH site) via through-bond interactions with Cu<sup>2+</sup>. This is supported by relative  $\Delta G^\circ$  calculations for the process Y'OH(H282<sup>-</sup>) → Y'O<sup>-</sup>(H282H), where  $\Delta G^\circ = -8.7 \pm 2.7$  and  $-6.5 \pm 3.7$  kcal mol<sup>-1</sup> for PW91 and B3LYP\*, respectively (average, range). This driving force strongly facilitates proton transfer from Y237 to H282. This average and range is based on our calculations for the tautomers of seven different states (5, 6, 9, 10, 11, 13, and 14; Figure 3), which are all Cu<sup>2+</sup> species.

From Figures 5B and 3, it is evident that the entire pathway from states 3 → 9<sub>2</sub> has only low-energy barriers, at least judging from the energy differences between these intermediates, and the overall pathway is highly exergonic, which is consistent with the rapid rate observed from states A → P<sub>R</sub> (observed as P<sub>I</sub>). The e<sup>-</sup> transfer from heme-b (Fe<sup>II</sup>) to the tyrosine radical P<sub>M</sub> → P<sub>R</sub> is clearly very fast, faster than 5 μs from experiment (Figure 2), and the earlier “true peroxo” intermediates are not observed (Figure 3). The calculated  $\Delta G^\circ$  value for 8H<sub>2</sub> → 9<sub>2</sub> is -23 kcal mol<sup>-1</sup> (corresponding to a redox potential of about +1.22 V; we assume that the redox potential of the donor is near that of cytochrome c, about 0.22 V). If the proton coming in must go to Y237 first, then  $\Delta G^\circ$  for tautomer 9<sub>1</sub> is more positive, -10.4 kcal mol<sup>-1</sup> (redox potential of about +0.67 versus SHE). However, this is still quite exergonic. For the next redox step, from state 11<sub>2</sub> to 12,  $\Delta G^\circ$  is again very negative, -21 kcal mol<sup>-1</sup> (redox potential of +1.12 V versus SHE). There are two coupled protonations assumed here, and it is assumed that e<sup>-</sup> transfer from heme-b Fe is to Cu<sup>II</sup> → Cu<sup>I</sup>. If state 12 is skipped in favor of state 13, so that e<sup>-</sup> transfer goes from heme-b Fe<sup>II</sup> to heme-a<sub>3</sub> Fe Fe<sup>IV</sup> → Fe<sup>III</sup> directly, the predicted  $\Delta G^\circ$  value is almost the same. The corresponding spectral state changes of the DNC are P<sub>R</sub> → F' and P<sub>R</sub> → O for reduction at Cu and Fe, respectively. As is seen in Figure 2, the transition from P<sub>R</sub> → O is observed to go fairly slowly, and P<sub>R</sub> → F' is not directly observed. Cu<sup>I</sup> is, however, not a good spectroscopic reporter using optical difference spectroscopy, and spectral analysis is focused on heme-a<sub>3</sub> Fe. Typically, the state F' is not seen in the normal reaction cycle of CcO but can be generated by binding H<sub>2</sub>O<sub>2</sub> to the reduced state R (Fe<sup>II</sup> and Cu<sup>I</sup>) in the

DNC. This shortcircuits the normal catalytic cycle, and the intermediate state F' slowly changes back to state O (resting oxidized).<sup>49,50</sup> In any event, the comparative slowness of the observed P<sub>R</sub> → O transition may well be a consequence of the coupled proton transfers and associated proton rearrangement. (All calculations above are with PW91, unless noted otherwise.)

**Large Model: Structures and Energies.** In Tables 1 and 2 (see also Figure 4, right), we present structures and energies for a number of states of the large model. We focus on two arcs with OLYP potential, one encompassing the “true peroxo” states (4 → 5 → 6), Table 1, and the second covering the last 1e<sup>-</sup> reduction ending in the resting state O (11<sub>2</sub> → 12 → 13 → 14 → 1; P<sub>R</sub> → F' → O), Table 2. The size of the quantum cluster is increased to 205–207 atoms by adding structural waters observed in the Tiefenbrunn X-ray structure and a glycine fragment that hydrogen bonds to internal waters near the reaction site. The larger size of the cluster allows us to model the reaction geometries with less constraints. The Fe–Cu distance is no longer constrained to X-ray geometries as in work by Fee et al.<sup>2</sup> Convergence of the electronic structure self-consistent field and geometries is improved. Also, the OLYP potential used typically has a better balance in describing the relative energies of different site spin states for Fe and typically yields more accurate spin coupling energies between transition-metal sites compared to PW91. In work by Fee et al. (2008),<sup>2</sup> we employed parallel spin on (ferromagnetic coupling, F) Fe and Cu sites for ease of computation and kept the observed experimental site spins over the reaction cycle. By contrast, the newer calculations take account of both F and AF (antiferromagnetic) alignment of the site spins, and different possible site spins as well (see Table 1), and our recent paper.<sup>37</sup>

In Tables 1 and 2, simple redox potentials without coupled protonation events can be calculated with the equation

$$E^\circ = (E_{\text{ox}} - E_{\text{red}}) + \Delta E(\text{SHE}) \quad (4)$$

where the absolute standard hydrogen electrode energy value is taken as  $\Delta E(\text{SHE}) = -4.34$  eV = -100.1 kcal mol<sup>-1</sup> and  $E_{\text{ox}}$  and  $E_{\text{red}}$  are the energies of the oxidized and reduced states.  $\Delta E(\text{SHE})$  corresponds to the best measured solvation free energy of a proton  $\Delta G_{\text{solv}} = -264.0$  kcal mol<sup>-1</sup>, where the ionization threshold energy of a free electron is taken as 0, with no account of electron entropy (see the Appendix and references therein). Similarly,  $\Delta G_{\text{deprot}}$  can be computed from ADF energies; we take a typical  $\Delta E(\text{ZPE})$  (ZPE = zero-point

Table 1. OLYP-Calculated Energies ( $E$ , offset by  $-27900 \text{ kcal mol}^{-1}$ ),  $S^2$  Expectation Value, Net Charge of the Cluster ( $Q$ ), and Key Geometric Data (Distances in Angstroms and Angles in Degrees) for Both F- and AF-Coupled Low-Spin  $\text{Fe}^{3+}\text{-Cu}^{2+}$  Compounds **4**, **5**, **5<sub>2</sub>**, **6**, **6H**, and **6<sub>2</sub>** with a Larger Model<sup>a</sup>

	$E^b$	O1–O2	Fe–O1	Fe–N(H384)	Cu–O2	Cu–N(H233)	Cu–N(H282)	Cu–N(H283)	Fe...Cu	O...O(Y237)	$\angle\text{Fe–O1–O2}$	$\angle\text{Fe–O1–O2–Cu}$	$S^2$	$Q$
<b>4</b>	F	–33.5	1.87	2.19	2.08	2.14	2.12	2.18	4.60	3.28	125	–137	2.04	0
	AF	–32.8 (+0.3)	1.82	2.29	2.07	2.19	2.13	2.12	4.40	3.21	121	–123	0.54	0
<b>5</b>	F	–35.1	1.87	2.20	2.03	2.10	2.12	2.17	4.42	2.77	115	–135	2.04	0
	AF	–35.2 (+0.0)	1.84	2.30	2.10	2.13	2.14	2.14	4.44	2.83	122	–123	0.61	0
<b>5<sub>2</sub></b>	F	–24.7	1.87	2.19	2.02	2.16	2.02	2.21	4.49	3.35	123	–135	2.04	0
	AF	–27.3 (–1.1)	1.82	2.27	2.07	2.23	2.03	2.19	4.39	3.40	122	–123	0.59	0
<b>6</b>	F	–26.4	1.77	2.18	2.35	2.08	2.06	2.11	4.78	3.10	117	–128	2.02	1
	AF	–28.5 (–2.2)	1.79	2.15	2.66	2.03	2.06	2.07	5.07	3.08	116	–134	1.02	1
<b>6H</b>	F	–19.0	1.82	2.13	2.64	2.03	2.06	2.03	5.07	3.41	115	–137	2.04	2
	AF	–15.0 (+1.7)	1.78	2.11	2.68	2.03	2.06	2.03	5.04	3.47	118	–125	0.6	2
<b>6<sub>2</sub></b>	F	–34.4	1.88	2.21	2.05	2.14	2.13	2.16	4.46	3.44	113	–136	2.04	1
	AF	–36.3 (–0.9)	1.83	2.24	2.10	2.18	2.14	2.14	4.45	3.47	121	–127	0.63	1

<sup>a</sup>Note that structure **4** of the larger model here does not have the water molecule above His376. O1 is the atom that is closer to the Fe site. <sup>b</sup>F stands for ferromagnetic coupling and AF for antiferromagnetic coupling. The energies given in the AF-coupled states are broken-symmetry state energies. The spin projection corrections ( $\text{kcal mol}^{-1}$ ) are given in parentheses.

energy) for deprotonation of hydroxyl oxygen as about  $-8.7 \text{ kcal mol}^{-1}$ , and this gives the protonation energy correction for single proton addition as  $-4.5 \text{ kcal mol}^{-1}$  at  $\text{pH} = 7$  (see the Appendix, Table A3). This is a DFT correction,  $-2.9 \text{ kcal mol}^{-1}$  plus an empirical correction ( $-1.6 \text{ kcal mol}^{-1}$ ), to the ADF energy differences  $E(\text{HA}) - E(\text{A}^-)$ , from Table 1. For different tautomers in Tables 1 and 2, energy differences are directly meaningful without correction, assuming only that  $\Delta E(\text{ZPE})$  cancels for deprotonation/protonation. In Table 1, we include the small spin projection energy corrections from the broken symmetry (AF) to the proper pure spin singlet states, in parentheses. From Table 1, state **4**, and ref 37,  $1e^-$  reduction of state **4** is very unfavorable, redox potential  $E^\circ = -0.73 \text{ V}$  vs SHE, so cytochrome *c* (or heme-b) cannot further reduce the  $\text{Fe}^{\text{III}}\text{-(O-O)}^{2-}\text{-Cu}^{\text{II}}$  complex. Protonation of state **6** at the tyrosine anion ( $\text{Y237}^-$ ) is very unfavorable ( $\Delta G_{\text{prot}} = 7.2 \text{ kcal mol}^{-1}$ , about 5.3 pH units more acid than  $\text{pH} = 7$ ), which is important because the tyrosine anion is well adapted to become a radical after  $1e^-$  transfer to  $\text{Fe}^{\text{III}}\text{-(OOH)}^-\text{-Cu}^{\text{II}}$ , which would be suppressed if the neutral tyrosine (YOH) were very stable. The reaction pathway **4**  $\rightarrow$  **5<sub>2</sub>**  $\rightarrow$  **5**  $\rightarrow$  **6<sub>2</sub>**  $\rightarrow$  **6** has  $\Delta G = +5.1, -6.8, -4.1$ , and  $+6.5 \text{ kcal mol}^{-1}$  and is similar to the energy profile for the smaller model S2. The protonation free energy for **5**  $\rightarrow$  **6<sub>2</sub>**  $-4.1 \text{ kcal mol}^{-1}$  includes an empirical correction (see the Appendix, Table A3). Structurally, it is clear that the hydroperoxide in state **6** is very important for breaking the O–O bond because the activated AF state has an O–O distance of  $1.49 \text{ \AA}$ . The calculated F-coupled state **6** has an even longer O–O bond,  $1.53 \text{ \AA}$ , and is only  $4.3 \text{ kcal mol}^{-1}$  above AF. Even more importantly, the Cu–O2 (bond to hydroperoxo O atom) bond is significantly shorter in the F state,  $2.35 \text{ \AA}$  compared to  $2.66 \text{ \AA}$  in the AF state, and is on the path to a  $\text{Cu}^{\text{II}}\text{-OH}$  structure after O–O bond breaking. The Fe–O1 bond is also close to that expected for ferryl oxo in both F and AF. Also, the charged  $a_3 \text{ ROH}\cdots\text{OY}^-$  hydrogen bond is very short,  $\text{O}\cdots\text{O} = 2.83 \text{ \AA}$  in state **5**, and still short in state **6** but much longer for all states with neutral Tyr–OH (Y237). This is entirely consistent with what we saw in ref 37, where the X-ray structure of Tiefenbrunn<sup>19</sup> was proposed to have a charged  $a_3 \text{ ROH}$  bond. Turning now to the reaction pathway for the final  $e^-$  transfer  $\text{P}_R \rightarrow \text{O}$ , it is clear that obtaining  $\text{Fe}^{\text{III}}\text{-OH}^-$  would be facilitated by having a nearby proton, but in the earlier small model (S2; Figure 3), we proposed that  $\text{H}_2\text{O}$  exited the reaction pocket directly between Fe and Cu at this stage. Instead, we now retain this scalar  $\text{H}_2\text{O}$  in states **12**  $\text{H}_2\text{O}$ , **13**  $\text{H}_2\text{O}$ , **14**  $\text{H}_2\text{O}$ , and **1**  $\text{H}_2\text{O}$  (F' and O). In place of state **11<sub>2</sub>** in Figure 3, we now add  $2\text{H}^+$  to form two tautomeric states (the first two lines in Table 2). We find that the addition of these two protons is very favorable and so should precede  $1e^-$  reduction. These two states are related by a proton shift from Y237 (YOH) to replace the proton shifted from  $\text{H}_2\text{O}\text{-Cu}^{\text{II}}$  to  $\text{Fe}^{\text{IV}}=\text{O}$ . Our calculations indicate that to some extent an electron may accompany this proton transfer onto the Fe, but this state is a resonance mixture of valence isomers. The proton-shifted tautomer **11<sub>2</sub>**  $2\text{H}^{\text{II}}$  (tautomer 1; Table 2, line 1) is lower in energy than **11<sub>2</sub>**  $2\text{H}^{\text{I}}$  (tautomer 2) by about  $5 \text{ kcal mol}^{-1}$ , while upon  $1e^-$  reduction, the  $\text{Cu}^{\text{I}}$  state is predicted to be lower, by about  $4 \text{ kcal mol}^{-1}$  ( $0.17 \text{ eV}$ ). The corresponding redox potential is about  $0.57 \text{ V}$  (reduction of Cu) or  $0.40 \text{ V}$  (reduction of Fe). The actual reduction process may not follow the lowest energies because it is favorable to preserve the proton shift to form  $\text{Fe-OH}^-$  once this is formed. Further, kinetic measurements of Farver, Fee, and co-workers<sup>27</sup>

Table 2. OLYP Calculations on Larger DNC Clusters in the Later Cycle with the Scalar Water on Cu<sup>+/2+</sup><sup>a</sup>

state <sup>b</sup>	geometry						<i>E</i>	<i>Q</i>	<i>S</i> <sup>2</sup>	net spin			
	Fe–N(H384)	Fe–O1	Cu–O2	O1...O2	Fe...Cu	O...O(Y237)				Fe <sup>3+</sup>	O1	O2	Cu <sup>2+</sup>
11 <sub>2</sub> _2H <sup>11</sup> (F) <sup>c</sup>	2.07	1.83	2.32	2.72	5.68	3.35	−49.26	2	3.79	1.29	0.15	0.02	0.37
11 <sub>2</sub> _2H <sup>12</sup> (F) <sup>d</sup>	2.18	1.66	2.06	2.65	5.24	3.32	−44.91	2	3.78	1.31	0.77	0.09	0.54
12_H <sub>2</sub> O (F) <sup>e</sup>	2.20	1.65	3.83	2.95	5.74	3.41	−162.48	1	2.02	1.23	0.84	0.01	0.00
13_H <sub>2</sub> O (F) <sup>f</sup>	2.07	1.84	2.39	2.67	5.55	3.12	−158.30	1	2.03	0.95	0.14	0.02	0.33
14_H <sub>2</sub> O (F) <sup>g</sup>	2.07	1.85	2.20	2.60	5.39	3.15	−155.05	0	2.02	1.01	0.13	0.02	0.34
14_H <sub>2</sub> O (AF) <sup>g</sup>	2.08	1.85	2.28	2.64	5.46	3.14	−156.36	0	1.02	−0.94	−0.13	0.02	0.34
1_H <sub>2</sub> O (F) <sup>h</sup>	2.07	1.84	2.44	2.68	5.57	3.10	−152.10	0	2.02	0.94	0.14	0.02	0.37
1_H <sub>2</sub> O (AF) <sup>h</sup>	2.07	1.84	2.43	2.68	5.57	3.10	−152.40	0	1.02	0.94	0.14	−0.02	−0.37

<sup>a</sup>OLYP calculations have been performed on the larger model. The calculated properties given here include energies (*E*, offset by −28000 kcal mol<sup>−1</sup>), *S*<sup>2</sup> expectation values, net charges of the cluster (*Q*), the Mulliken net spin polarizations for the Fe, Cu, O1, and O2 atoms, and the key geometric data (distances in angstroms). <sup>b</sup>F stands for ferromagnetic coupling and AF for antiferromagnetic coupling. In the following notes, LS represents low spin and IS represents intermediate spin. <sup>c</sup>Formally adding two protons to state 11<sub>2</sub>, one on the H282<sup>−</sup> side chain and another one on Fe<sup>4+</sup>=O<sup>2−</sup>. This is tautomer 1 (t1) of 11<sub>2</sub>\_2H with lower energy (see footnote d for tautomer 2). The optimized structure is a mixed state of Fe<sup>3+,LS</sup>–OH<sup>−</sup>...H<sub>2</sub>O–Cu<sup>2+</sup>(H376H<sup>+</sup>,H282H,Y237<sup>•</sup>), Fe<sup>4+,IS</sup>–OH<sup>−</sup>...H<sub>2</sub>O–Cu<sup>2+</sup>(H376H<sup>+</sup>,H282H,Y237<sup>−</sup>), and Fe<sup>4+,IS</sup>–OH<sup>−</sup>...H<sub>2</sub>O–Cu<sup>+</sup>(H376H<sup>+</sup>,H282H,Y237<sup>•</sup>). The calculated net spin on the Y237<sup>•</sup> side chain is 0.93. <sup>d</sup>State Fe<sup>4+,IS</sup>=O...H<sub>2</sub>O–Cu<sup>2+</sup>(H376H<sup>+</sup>,H282H,Y237<sup>−</sup>). This is the second tautomer (t2) of state 11<sub>2</sub>\_2H with higher energy. <sup>e</sup>State Fe<sup>4+,IS</sup>=O...H<sub>2</sub>O...Cu<sup>+</sup>(H376H<sup>+</sup>,H282H,Y237<sup>−</sup>). This is formal state 12 + H<sub>2</sub>O, where H<sub>2</sub>O is scalar water on Cu<sup>+</sup>. <sup>f</sup>State Fe<sup>3+,LS</sup>–OH<sup>−</sup>...H<sub>2</sub>O–Cu<sup>2+</sup>(Y237<sup>−</sup>). This is formal state 13 + H<sub>2</sub>O. <sup>g</sup>State Fe<sup>3+,LS</sup>–OH<sup>−</sup>...H<sub>2</sub>O–Cu<sup>2+</sup>(H376H<sup>+</sup>,H282H,Y237<sup>−</sup>). Note that in this larger model no water molecule is added on the top of H376. <sup>h</sup>State Fe<sup>3+,LS</sup>–OH<sup>−</sup>...H<sub>2</sub>O–Cu<sup>2+</sup>(H376H<sup>+</sup>,H282<sup>−</sup>,Y237<sup>−</sup>). Spin projection corrections are: −1.3, −0.3 kcal mol<sup>−1</sup> for 14\_H<sub>2</sub>O (AF) and 1\_H<sub>2</sub>O (AF).

implicate total reorganization energies in the range of 1.0–1.5 eV for e<sup>−</sup> transfer between heme-b and heme-a<sub>3</sub> Fe. Both the driving force and the reorganization energies then are important for the timing of e<sup>−</sup> transfer.

The Fe<sup>III</sup>–OH<sup>−</sup>...H<sub>2</sub>O–Cu<sup>II</sup> state (13\_H<sub>2</sub>O) will provide a focal point for the last part of the reaction cycle (second arc) extending from 11<sub>2</sub>\_2H → 13\_H<sub>2</sub>O → 14\_H<sub>2</sub>O → 1\_H<sub>2</sub>O. In Figure 8, we present the energy profile from the last 1e<sup>−</sup>

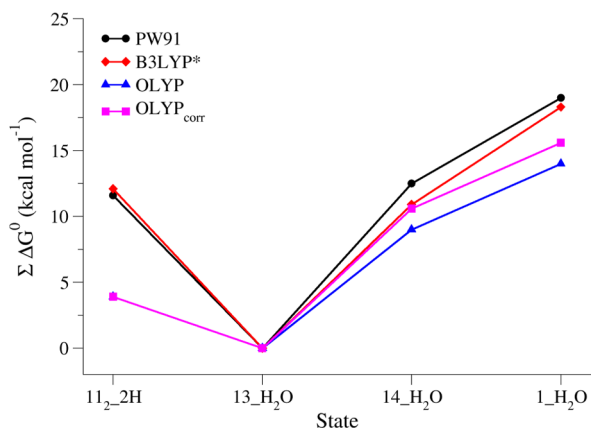


Figure 8. Plots of  $\Sigma\Delta G^\circ$  (kcal mol<sup>−1</sup>) relative to state 13\_H<sub>2</sub>O along the trajectory from 11<sub>2</sub>\_2H (lower energy tautomer 1) to 1\_H<sub>2</sub>O in the cycle with the scalar water on Cu<sup>II</sup>. The PW91 and B3LYP\* energies were obtained for the smaller model (see Table S2 in the Supporting Information, SI). OLYP calculations were performed on the larger models (Tables 2 and A3).

reduction to the last proton pumping as assumed within the model cycle to the final reset to the initial state 1. We also compare the energetic pathway with one where the scalar H<sub>2</sub>O on Cu<sup>II</sup> has dissociated (Figure 9). Typically, the energy profile is similar to that without H<sub>2</sub>O. However, the presence of H<sub>2</sub>O on Cu<sup>II</sup> facilitates proton transfer between Cu<sup>II</sup>–H<sub>2</sub>O and Fe<sup>IV</sup>=O<sup>2−</sup> or Fe<sup>III</sup>–OH<sup>−</sup>. Further, there is recent X-ray structural evidence for two waters or OH<sup>−</sup>–H<sub>2</sub>O between Fe<sup>III</sup> and Cu<sup>II</sup> in the resting state O.<sup>19,37</sup> We do find that

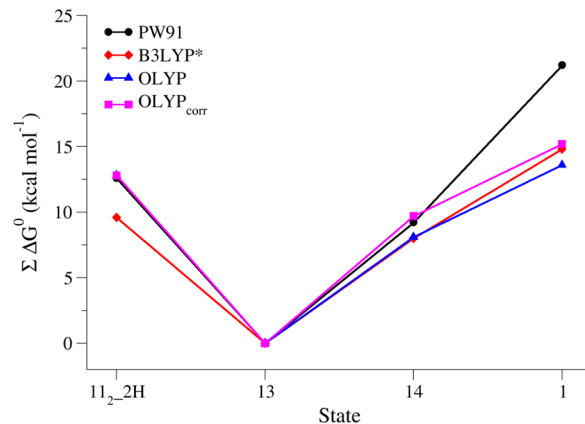


Figure 9. Plots of  $\Sigma\Delta G^\circ$  (kcal mol<sup>−1</sup>) relative to state 13\_H<sub>2</sub>O along the trajectory from 11<sub>2</sub>\_2H to 1 in the cycle without the scalar water on Cu<sup>II</sup>. The PW91 and B3LYP\* energies were obtained for the smaller model (see Tables S2 and S3 in the SI). OLYP calculations were performed on the larger models (Tables 3 and A3).

$\Delta G(\text{H}_2\text{O dissociation}) = -9$  kcal mol<sup>−1</sup> (OLYP), favoring dissociation, and less, −0.6 kcal mol<sup>−1</sup> (PW91) and +3.2 kcal mol<sup>−1</sup> (B3LYP\*), but based on the active site structure, kinetic trapping for the Cu<sup>II</sup>-bound H<sub>2</sub>O is likely. Two waters are probably released after 2e<sup>−</sup> reduction of state 1\_H<sub>2</sub>O → 2H (O → R) with a lowering of the free energy.<sup>18,19,37</sup> This conclusion is supported by X-ray structural evidence.

Returning to the energy profiles in Figure 8, the calculated  $\Sigma\Delta G^\circ$  values for 1\_H<sub>2</sub>O relative to state 13\_H<sub>2</sub>O are +14.0 and +15.6 kcal mol<sup>−1</sup> for the large OLYP model (without and with the empirical deprotonation correction) and +19.0 and +18.3 kcal mol<sup>−1</sup> for PW91 and B3LYP\*. In Figure 9, the corresponding energies are +13.6, +15.2, +21.2, and +14.8 kcal mol<sup>−1</sup> for OLYP, OLYP<sub>corr</sub>, PW91, and B3LYP\*. These are not high energy differences for proton pumping considering that a +5.5 kcal mol<sup>−1</sup> pumping cost (for pH = 7 → pH = 3) is included.

**Bifurcation Points, Chemical and Vector Protons, and the Exit Pathway.** In light of the experimental structural,



kinetics, and mutagenesis data for  $\text{ba}_3$  from *Tt*, the idea that there is a largely common pathway for scalar and vector protons and that this derives from the  $\text{K}_\text{B}$  pathway should not be surprising. We can see two reasonable bifurcation points. The first, mentioned earlier (see Figure 6), is at  $\text{a}_3\text{-ROH}$  and the adjacent Tyr237. This bifurcation point is mainly utilized as needed to bypass Tyr237 when it is in a radical state, and a proton needs to be passed on, especially a chemical proton entering the reaction chamber between Fe and Cu at that stage. The other bifurcation point, which we think is much more common in the reaction path, occurs at His282. From this location, a proton on His282 (neutral) can move onto a  $\text{Cu}^{\text{II}}$ -bound hydroxo or peroxy (scalar proton), with the different tautomers being close in energy from our DFT calculations. Alternatively, a vector proton can move onto the exit position (PLS) and proceed on the exit pathway. Specifically, starting with His282<sup>−</sup>, a proton enters typically from Tyr237 to generate His282 neutral. This will weaken the hydrogen bond to threonine (T302), allowing its side chain to rotate and deposit a proton on His376 or more probably in the nearby water pool (see Figure 4, large model, right). (This location is near propionate A, as previously proposed for the PLS location.) Above His376 in Figures 3 and 4 is an Asp287–Arg225 salt bridge. Catalytic turnover, proton pumping, and mutagenesis studies of Chang et al.<sup>28</sup> indicate that Asp287 is probably important for efficient proton pumping; these results are still incomplete, and only one mutation has been examined for Arg225, which is so far inconclusive. We propose that the Asp287–Arg225 salt bridge is potentially a simple electrostatic switch or gate, which could be opened by a strongly positive electrostatic potential nearby, for example, by having a proton in the adjacent water pool. The energy barrier to rupturing the Asp–Arg salt bridge could be paid when the proton enters the water pool or during transit. Also, the local electric field of this proton (and from the surrounding charge distribution) possibly acts in opposition to the long-range electric field from the membrane potential. This model is currently under study.

## CONCLUSIONS

On the basis of our earlier work on the catalytic cycle of the cytochrome  $\text{ba}_3$  DNC, we have found an improved reaction path by modifying the sequence of proton uptake and proton-transfer events and examining alternative tautomeric states. The new 14-step reaction cycle results in a much “smoother” energy pathway for the catalytic reaction cycle, comparing parts A and B of Figure 5 with lower barriers between intermediates. The entire pathway from state 3 → 9<sub>2</sub> has low-energy barriers and proceeds downhill. We have also tracked the DFT-calculated dipole moments of peroxy and hydroperoxy intermediates after  $\text{O}_2$  binding (Figure 7). Here we find that there are very substantial changes in the magnitude and direction of the dipole moment of the DNC with tautomeric shifts, and a progressive increase in the positive electrostatic potential near His376 (in addition to that due to protonation of His376 itself). We then constructed large model structures and evaluated geometries and energies (OLYP potential) for two arcs of the cycle, one for “true peroxy” states 4 → 5 → 6 and the other for the last  $1\text{e}^-$  reduction from state 11<sub>2</sub> → 1 (spectroscopic states  $\text{P}_\text{R}$  → O). Important results from these DFT calculations are presented in Figures 8 and 9 and Tables 2 and 3. We have tested the effect of keeping the scalar water bound to  $\text{Cu}^{\text{II}}$  in state 11<sub>2</sub> through the remainder of the catalytic cycle both for the large model (OLYP potential) and

**Table 3.** OLYP Calculations on Larger DNC Clusters in the Later Cycle without the Scalar Water on  $\text{Cu}^{+/2+}$ <sup>a</sup>

state <sup>b</sup>	<i>E</i>	<i>Q</i>	<i>S</i> <sub>2</sub>	net spin	
				$\text{Fe}^{2+/3+/4+}$	$\text{Cu}^{2+/+}$
11 <sub>2</sub> (F)	−28052.20	0	3.78	1.28	0.42
12	−27838.93	1	2.02	1.20	0.00
13 (F)	−27836.04	1	2.03	1.12	0.18
13 (AF)	−27835.24	1	1.04	0.94	−0.22
14 (F) <sup>c</sup>	−27836.30	0	2.03	1.14	0.19
14 (AF) <sup>c</sup>	−27836.23	0	1.03	0.94	−0.21
1 (F)	−27830.82	0	2.03	1.09	0.25
1 (AF)	−27829.53	0	1.03	0.93	−0.25
2H	−27708.87	1	6.22	3.84	0.00

<sup>a</sup>OLYP calculations have been performed on the larger model. The calculated properties given here include energies (*E* in kcal mol<sup>−1</sup>), *S*<sup>2</sup> expectation values, net charges of the cluster (*Q*), and the Mulliken net spin polarizations for Fe and Cu sites. <sup>b</sup>F stands for ferromagnetic coupling and AF for antiferromagnetic coupling. <sup>c</sup>Note that in this larger model no water molecule is added on the top of H376.

for the smaller model (PW91 and B3LYP\*) potentials. The energy profiles in both Figures 8 and 9 are similar, but the water on  $\text{Cu}^{\text{II}}$  facilitates protonation of Fe-oxo. The energy barriers for the final proton-pumping step 13 → 1 are about 15–16 kcal mol<sup>−1</sup> for OLYP, large model, and somewhat higher for B3LYP\* (15–18 kcal mol<sup>−1</sup> for B3LYP\*, small model) and for PW91 (19–21 kcal mol<sup>−1</sup>). These results include an assumed 5.5 kcal mol<sup>−1</sup> cost for proton pumping at one step. Further, we discuss a potential proton exit pathway involving breaking of an Asp–Arg salt bridge. The exiting proton would be carried or transferred via a water pool from inside to outside. Earlier on the vector proton pathway, we have proposed that His282 and Thr302 play an important role.

There are many important issues still to be understood in the reaction cycle and proton-pumping mechanism of CcO both in  $\text{ba}_3$  class enzymes and more broadly including also  $\text{aa}_3$  enzymes (bacterial and mitochondrial). We have not yet addressed the kinetics in detail, including transition states, effects of sequence differences, and mutational effects. The proton exit path from the DNC is probably complex.<sup>28</sup> More needs to be done to integrate the  $\text{K}_\text{B}$  path and the other redox centers into the models presented here. The scalar water exit pathway is also essential for proper analysis. In general, however, we expect that the structural and energetic maps of the reaction cycle in the DNC that we have generated will contribute to a better representation of the coupling of electron and proton transfer to proton pumping in CcO.

## APPENDIX

### Reference Energies for $\text{pK}_\text{a}$ Values and Related Free Energies

As a general equation for microscopic  $\text{pK}_\text{a}$  values, we use

$$\text{pK}_\text{a} = \{[E(\text{A}^-) - E(\text{HA})] + \Delta G_\text{ref}(\text{H}^+) + \Delta \text{ZPE}\} / 1.37 \quad (\text{A1})$$

where  $E(\text{A}^-)$  and  $E(\text{HA})$  are the calculated energies of the deprotonated and protonated states. The term  $\Delta \text{ZPE}$  is the zero-point-energy difference for the deprotonated state ( $\text{A}^-$ ) minus the protonated state ( $\text{HA}$ ) and is therefore negative. The term  $\Delta G_\text{ref}(\text{H}^+)$  accounts for the free energy of the titrating proton using eq A2:<sup>51</sup>

$$\Delta G_{\text{ref}}(\text{H}^+) = E(\text{H}^+) + \Delta G_{\text{sol}}(\text{H}^+, 1 \text{ atm}) - T\Delta S_{\text{gas}}(\text{H}^+) + (5/2)RT \quad (\text{A2})$$

The energies  $E(\text{A}^-)$  and  $E(\text{HA})$  follow the standard convention with the ADF codes, where  $E(\text{A}^-)$  and  $E(\text{HA})$  are “total” energies with respect to a sum of atomic fragments (spin-restricted atoms). In eq A2, the calculated energy of a proton  $E(\text{H}^+)$  is obtained from a gas-phase OLYP (or other exchange-correlation potentials) calculation with respect to a spin-restricted H atom. This result arises because the reference state adds one spin-restricted H atom when the state is protonated. In eq A2, the calculated energy of a proton,  $E(\text{H}^+)$ , is +291.4 kcal mol<sup>-1</sup> from a gas-phase OLYP calculation with respect to a spin-restricted H atom (ionization of a spin-restricted H atom). For  $\Delta G_{\text{sol}}(\text{H}^+, 1 \text{ atm})$ , the solvation free energy of a proton, we use the “best available” experimental value of -264.0 kcal mol<sup>-1</sup>, based on analysis of the cluster-ion solvation data. The free-energy term corresponding to the translational entropy of a proton,  $-T\Delta S_{\text{gas}}(\text{H}^+) = -7.8 \text{ kcal mol}^{-1}$ , computed from theory at 298 K and 1 atm. The final term  $(5/2)RT$  arises from the sum of the proton translational energy and  $PV = RT$ . We obtain the free energy of deprotonation at pH = 7 by using eq A1 and correcting for the proton concentration

$$\Delta G_{\text{deprot}} = 1.37(\text{pK}_{\text{a}} - 7) = [E(\text{A}^-) - E(\text{HA})] + [\Delta G_{\text{ref}}(\text{H}^+) + \Delta \text{ZPE} + \Delta E_{\text{corr}}(\text{pH} = 7)] \quad (\text{A3})$$

where  $\Delta E_{\text{corr}}(\text{pH} = 7) = -1.37 \times 7 = -9.6 \text{ kcal mol}^{-1}$  for a neutral solvent at pH = 7. Often,  $\Delta G_{\text{prot}}$  (for protonation) is more relevant, where  $\Delta G_{\text{prot}} = -\Delta G_{\text{deprot}}$ .

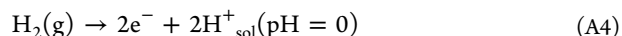
The zero-point-energy difference,  $\Delta \text{ZPE}$ , depends on the site being protonated (or deprotonated). For acetic acid deprotonation, we have calculated  $\Delta \text{ZPE} = -8.7 \text{ kcal mol}^{-1}$  and a very similar energy for the weakest bound proton of a pyrophosphate group. We will then take  $\Delta \text{ZPE} = -8.7 \text{ kcal mol}^{-1}$  as typical for the titrating sites in the DNC, whether tyrosine (OH) or histidine (NH) or bound hydroperoxide (OOH<sup>-</sup>). This approach simplifies the energy accounting for protonation (or deprotonation) from solution and eliminates the  $\Delta \text{ZPE}$  energy differences for transitions between different tautomers. We also note that the  $\Delta \text{ZPE}$  calculated for methylimidazole → imidazolate is -8.0 kcal mol<sup>-1</sup>, calculated with a PW91 potential.<sup>51,52</sup> ( $\Delta \text{ZPE}$  results are quite insensitive to the exchange-correlation potential used.) In our earlier paper,<sup>2</sup> we used  $\Delta \text{ZPE}$  for the average OH bond in H<sub>2</sub>O, -6.6 kcal mol<sup>-1</sup>, for all deprotonations (+6.6 kcal mol<sup>-1</sup> for all protonations) at all titrating sites. Because it is computationally very expensive to include  $\Delta \text{ZPE}$  computations on large intermediates, the  $\Delta \text{ZPE}$  terms are computed separately for deprotonations (protonations) and simply added in as needed. For the scalar water (H<sub>2</sub>O)<sub>s</sub> product, the ZPE energy is omitted because the  $\Delta \text{ZPE}$ 's are accounted for (approximately) as the water-OH covalent bonds are formed.

#### Empirical Correction to $E(\text{H}^+)$ and Connection to the Standard Hydrogen Electrode State

This section has the purpose of showing how the standard hydrogen electrode energy,  $\Delta E(\text{SHE})$ , and the proton solvation free energy,  $\Delta G_{\text{sol}}(\text{H}^+)$ , are connected and how referencing to the experimental  $\Delta G_{\text{sol}}(\text{H}^+)$  and  $\Delta E(\text{SHE})$  can be used to find a small, but not negligible, empirical correction to the proton energy  $E(\text{H}^+)$ . Because eqs A2 and A3 allow calculation of the protonation or deprotonation energies of titrating sites, this

empirical correction will have a moderate effect on these energies. The relevant method was already used in our 2008 paper (see Appendix A therein), but we have now recomputed these corrections for the initial exchange-correlation potentials PW91, OPBE, B3LYP, and B3LYP\*, correcting earlier errors and inconsistencies. It turns out that there are compensating errors here, so using the new proper  $\Delta E_{\text{corr}}(\text{H}^+)$  gives very small effects on  $\Delta G_{\text{deprot}}$  compared to the earlier results including corrections. We have also computed the new empirical correction for the OLYP exchange-correlation potential. In eq A2,  $\Delta E(\text{H}^+)$  shifts  $E(\text{H}^+)$  more positive by +1.6 kcal mol<sup>-1</sup> (+0.07 eV), which, in turn, stabilizes the protonation free energy ( $\Delta G_{\text{prot}}$ ) by -1.6 kcal mol<sup>-1</sup> and conversely destabilizes  $\Delta G_{\text{deprot}}$  by +1.6 kcal mol<sup>-1</sup>.

The standard hydrogen electrode equation is



This can be considered as either a deprotonation equation or an oxidation equation because it is both. However, it is a distinctive deprotonation equation because only one bond is broken to yield  $2\text{H}^+$  in solution. The corresponding general redox potential equation is

$$E^\circ = (G_{\text{ox}} - G_{\text{red}}) + \Delta E(\text{SHE}) \quad (\text{A5})$$

where for the SHE  $E^\circ = 0$ , so

$$G_{\text{ox}} - G_{\text{red}} = -\Delta E(\text{SHE}) \quad (\text{A6})$$

Our standard absolute SHE energy is  $\Delta E(\text{SHE}) = -4.34 \text{ V}$  equivalent to -100.1 kcal mol<sup>-1</sup> per electron with the convention that  $G(\text{e}^-) = 0 \text{ eV}$  exactly at the ionization threshold. This is a consistent convention that we use in all of our calculations. By contrast, Truhlar, Cramer, and co-workers<sup>53–55</sup> use an alternate consistent convention including also an electron entropy term  $-T\Delta S(\text{e}^-)$  and find  $\Delta E(\text{SHE}) = -4.28 \text{ eV}$ . The  $\Delta E(\text{SHE})$  reference energy is experimentally tied to the experimental  $\Delta G_{\text{sol}}(\text{H}^+, 1 \text{ atm})$  discussed above. Starting from eq A6

$$2\Delta G(\text{H}^+)_{\text{sol}}(\text{pH} = 0) + [2G(\text{H}^+)_{\text{g}} - G(\text{H}_2)_{\text{g}}] = -2\Delta E(\text{SHE}) \quad (\text{A7})$$

The second term

$$2\Delta G_{\text{g}}^\circ = [2G(\text{H}^+)_{\text{g}} - G(\text{H}_2)_{\text{g}}] \quad (\text{A8})$$

is experimentally known from gas-phase thermochemistry  $\Delta G_{\text{g}}^\circ = +15.79 \text{ eV}$  (364.1 kcal mol<sup>-1</sup>) and  $\Delta G(\text{H}^+)_{\text{sol}}(\text{pH} = 0)$  also determined experimentally. Equation A8 is compared with its DFT-calculated counterpart, and  $E(\text{H}^+)$  is corrected accordingly.

From eqs A7 and A8,

$$\Delta G_{\text{g}}^\circ = -\Delta G(\text{H}^+)_{\text{sol}} - \Delta E(\text{SHE}) \quad (\text{A9})$$

Also  $\Delta G_{\text{g}}^\circ$  can be related to the result from DFT

$$\Delta G_{\text{g}}^\circ = [E(\text{H}^+) + \Delta E_{\text{corr}}(\text{H}^+) - TS(\text{H}^+)_{\text{gas}} + (5/2)RT] - (1/2)G(\text{H}_2)_{\text{g}} \quad (\text{A10})$$

The procedure is then to calculate  $E(\text{H}^+)$  and  $G(\text{H}_2)_{\text{g}}$  from DFT. To obtain the empirical correction to the DFT result, we can use the experimental  $\Delta G_{\text{g}}^\circ$  and compute  $\Delta E_{\text{corr}}(\text{H}^+)$  from eq A10. Then in eqs A1–A3, we substitute the value of  $E(\text{H}^+) + \Delta E_{\text{corr}}(\text{H}^+)$  for  $E(\text{H}^+)$ . From the experimental side, the

fundamental quantities are  $\Delta G_g^\circ$  and  $\Delta G(H^+)_{\text{sol}}$  and then  $\Delta E(\text{SHE})$  is computed from eq A9.

From eq A10, we calculate  $\Delta E_{\text{corr}}(H^+)$  for OLYP and recalculate it also for the other exchange-correlation potentials (PW91, OPBE, B3LYP, and B3LYP\*). The resulting values are given in Table A1.

**Table A1. Empirically (emp) Corrected  $E(H^+)$  (eV)**

potential	$E(H^+)$	$\Delta E_{\text{corr}}(H^+)$	final $E(H^+)$	$\Delta G_{\text{prot,shift}}(\text{emp})$ (kcal mol <sup>-1</sup> )
OLYP	12.64	+0.07	12.71	-1.6
PW91	12.51	+0.13	12.64	-3.0
OPBE	12.64	0.00	12.64	0.0
B3LYP	12.11	+0.13	12.24	-3.0
B3LYP*	12.17	+0.19	12.36	-4.4

In our earlier paper,<sup>2</sup> the final  $E(H^+)$  values are uniformly less than those in Table A1 for PW91 by 0.07–0.08 eV (and also for OPBE, B3LYP, and B3LYP\*), but this is almost entirely due to using a less accurate value for  $\Delta G_{\text{sol}}(H^+) = -262.1$  kcal mol<sup>-1</sup> (from previous DFT calculations)<sup>2,56</sup> instead of the current  $\Delta G_{\text{sol}}(H^+) = -264.0$  kcal mol<sup>-1</sup>.<sup>55</sup> Further, in that paper, we used  $\Delta E(\text{SHE}) = -4.36$  V (–100.5 kcal mol<sup>-1</sup>) instead of the current value  $\Delta E(\text{SHE}) = -4.34$  V (–100.1 kcal mol<sup>-1</sup>). In that paper,  $\Delta E_{\text{corr}}(H^+)$  was computed from the right-hand side of eq A9 substituted into eq A10, which is then solved for  $\Delta E_{\text{corr}}(H^+)$ . Consequently, in the relevant eqs A2 and A3, the different final  $E(H^+)$  values are almost exactly compensated for by the difference in  $\Delta G_{\text{sol}}$ . As seen in Table A1, use of eqs A2 and A3 shows that changing  $E(H^+)$  to  $E(H^+) + \Delta E_{\text{corr}}(H^+)$  gives  $\Delta G_{\text{prot,shift}}(\text{emp}) = -\Delta E_{\text{corr}}(H^+)$ .

Clearly, the procedure discussed above makes the standard hydrogen electrode match experiment perfectly, but is this more broadly valuable? The effect for OLYP is about –1.6 kcal mol<sup>-1</sup> for protonation, which is significant particularly when one considers the full thermochemical or catalytic cycle involving four protons added net [ $4\Delta G_{\text{prot,shift}}(\text{emp}) = -6.4$  kcal mol<sup>-1</sup>, for OLYP] and with protons entering and leaving the catalytic cycle. We established previously that the net thermochemical cycle energies for the different exchange-correlation potentials are more consistent when this correction is included (see Table A2).

We note that the first equation in Table A2 has the same number of bonds made as broken, similar to an isodesmic reaction. The electrochemical equation can be converted to the gas-phase equation by adding the standard hydrogen electrode eq A4 twice, converting standard states, and omitting the pumping cost. (In the electrochemical equation, we used the redox potential for cytochrome *c* as 0.22 V vs SHE,<sup>7</sup> and  $\Delta E(\text{SHE}) = -4.34$  V.)

**Table A2. Reaction Free Energies for Five Different Exchange Correlation Potentials**

reaction	PW91	OLYP	OPBE	B3LYP	B3LYP*	Exp
$O_2(\text{gas}) + 2H_2(\text{gas}) \rightarrow 2H_2O(\text{gas})$	–99.9	–91.1	–93.6	–97.2	–96.1	–109.3
$O_2(\text{aq}) + 4e^-$ (from cyt <i>c</i> ) + $8H^+(\text{aq}, \text{pH}=7) \rightarrow 2H_2O(\text{liquid}) + 4H^+(\text{aq}, \text{pH}=3)^a$	–27.3 (–15.3)	–19.2 (–12.8)	–21.4 (–21.4)	–26.2 (–14.2)	–24.7 (–7.1)	–36.9
$4\Delta G_{\text{prot,shift}}(\text{emp})^b$	–12.0	–6.4	0.0	–12.0	–17.6	

<sup>a</sup>Corrected energies are given without parentheses, and uncorrected energies are in parentheses. <sup>b</sup> $4\Delta G_{\text{prot,shift}}(\text{emp})$  is the total protonation free-energy empirical correction for  $4H^+$  added to  $O_2$ , forming  $2H_2O$ .

Compared to Table 3 and eq 4 in ref 2, Table A2 contains small energy corrections using Table A1 for PW91, OPBE, B3LYP, and B3LYP\*. The experimental  $\Delta G = -36.9$  kcal mol<sup>-1</sup> corresponds to a cytochrome *c* redox potential of +0.22 V.<sup>7</sup>

More generally, it is useful to define the second term in eq A3 as a separate quantity

$$\Delta G_{\text{deprot,shift}} = [\Delta G_{\text{ref}}(H^+) + \Delta \text{ZPE} + \Delta E_{\text{corr}}(\text{pH} = 7)] \quad (\text{A11})$$

or for protonation  $\Delta G_{\text{prot,shift}} = -\Delta G_{\text{deprot,shift}}$ . Using the DFT-calculated  $E(H^+)$  in eq A2 gives  $\Delta G_{\text{prot,shift}}(\text{DFT})$ . The effect of the empirical correction to  $E(H^+)$  gives term  $\Delta G_{\text{prot,shift}}(\text{emp}) = -\Delta E_{\text{corr}}(H^+)$ . The sum is  $\Delta G_{\text{prot,shift}}(\text{final}) = \Delta G_{\text{prot,shift}}(\text{DFT}) + \Delta G_{\text{prot,shift}}(\text{emp})$ . Then eq A3 can be more easily calculated:

$$\Delta G_{\text{deprot}} = [E(A^-) - E(\text{HA})] + \Delta G_{\text{deprot,shift}} \quad (\text{A12})$$

Similarly,

$$\Delta G_{\text{prot}} = [E(\text{HA}) - E(A^-)] + \Delta G_{\text{prot,shift}} \quad (\text{A13})$$

In Table A3, we collect the  $\Delta G_{\text{prot,shift}}$  term energies for the five different exchange-correlation potentials. With this

**Table A3.  $\Delta G_{\text{prot,shift}}$  Calculations (kcal mol<sup>-1</sup>)**

potential	$\Delta G_{\text{prot,shift}}$		
	DFT	emp	final
OLYP <sup>a</sup>	–2.9	–1.6	–4.5
OLYP <sup>b</sup>	–5.2	–1.6	–6.8
PW91 <sup>c</sup>	–2.0	–3.0	–5.0
OPBE <sup>c</sup>	–5.0	0.0	–5.0
B3LYP <sup>c</sup>	+7.2	–3.0	+4.2
B3LYP* <sup>c</sup>	+5.6	–4.4	+1.2

<sup>a</sup> $\Delta G_{\text{prot,shift}}(\text{DFT})$  depends on  $-\Delta \text{ZPE}$ . Here  $-\Delta \text{ZPE} = +8.7$  kcal mol<sup>-1</sup> for use in the catalytic reaction cycle for OLYP. <sup>b</sup> $-\Delta \text{ZPE} = +6.5$  kcal mol<sup>-1</sup> from the average OH bond ZPE for  $H_2O$  in OLYP. For use in Table A2. <sup>c</sup> $-\Delta \text{ZPE} = +6.6$  kcal mol<sup>-1</sup> for all other potentials for both the catalytic reaction cycle and thermochemistry in Table A2.

completed, evaluating eqs A12 or A13 is simpler with  $E(A^-)$  and  $E(\text{HA})$  as DFT-calculated inputs and using the look up Table A3.

## ■ ASSOCIATED CONTENT

### Supporting Information

Cartesian coordinates of the OLYP-optimized larger clusters in Tables 1–3 and the PW91-optimized smaller models discussed in this paper, some additional energy comparisons for different states/tautomers, and the structures of the original states **1–14** in the Fee et al. 2008 paper.<sup>2</sup> This material is available free of charge via the Internet at <http://pubs.acs.org>.



## ■ AUTHOR INFORMATION

## Corresponding Author

\*E-mail: lou@scripps.edu.

## Notes

The authors declare no competing financial interest.

## ■ ACKNOWLEDGMENTS

This paper is in memory of Jim Fee and his many critical contributions to the field of CcO. He is also a coauthor of this paper because he made major contributions both to the DFT calculations we have presented here and to the underlying framework of these studies, including extensive experimental work on the kinetics, spectroscopies, and X-ray structures. We are grateful also for valuable discussions of central issues with Prof. C. David Stout and Prof. Olaf Einarsdottir and for earlier discussions with Prof. Per Siegbahn. We thank the Scripps Research Institute for computational resources. We thank the NIH for financial support (Grant R01 GM100934). This work also used the Extreme Science and Engineering Discovery Environment (XSEDE), supported by National Science Foundation grant ACI-1053575. We appreciate computer time from the San Diego Supercomputer Center through XSEDE award TG-CHE130010.

## ■ REFERENCES

- (1) Korzybski, A. *Science and Sanity* 1933, 747–761.
- (2) Fee, J. A.; Case, D. A.; Noodleman, L. *J. Am. Chem. Soc.* **2008**, *130*, 15002–15021.
- (3) Richter, O. M. H.; Ludwig, B. *Rev. Physiol. Biochem. Pharmacol.* **2003**, *147*, 47–74.
- (4) Babcock, G. T.; Wikström, M. *Nature* **1992**, *356*, 301–309.
- (5) Ferguson-Miller, S.; Babcock, G. T. *Chem. Rev.* **1996**, *96*, 2889–2907.
- (6) Malmström, B. G. *J. Biol. Inorg. Chem.* **1998**, *3*, 339–343.
- (7) Nicholls, D. G.; Ferguson, S. J. *Bioenergetics 3*; Academic Press: San Diego, CA, 2002.
- (8) Siletsky, S. A.; Belevich, I.; Jasaitis, A.; Konstantinov, A. A.; Wikström, M.; Soulimane, T.; Verkhovskiy, M. I. *Biochim. Biophys. Acta* **2007**, *1767*, 1383–1392.
- (9) Muramoto, K.; Hirata, K.; Shinzawa-Itoh, K.; Yoko-O, S.; Yamashita, E.; Aoyama, H.; Tsukihara, T.; Yoshikawa, S. *Proc. Natl. Acad. Sci. U. S. A.* **2007**, *104*, 7881–7886.
- (10) Liu, J. A.; Qin, L.; Ferguson-Miller, S. *Proc. Natl. Acad. Sci. U. S. A.* **2011**, *108*, 1284–1289.
- (11) Blomberg, M. R. A.; Borowski, T.; Himo, F.; Liao, R. Z.; Siegbahn, P. E. *Chem. Rev.* **2014**, *114*, 3601–3658.
- (12) Hunsicker-Wang, L. M.; Pacoma, R. L.; Chen, Y.; Fee, J. A.; Stout, C. D. *Acta Crystallogr., Sect. D: Biol. Crystallogr.* **2005**, *61*, 340–343.
- (13) Luna, V. M.; Chen, Y.; Fee, J. A.; Stout, C. D. *Biochemistry* **2008**, *47*, 4657–4665.
- (14) Iwata, S.; Ostermeier, C.; Ludwig, B.; Michel, H. *Nature* **1995**, *376*, 660–669.
- (15) Soulimane, T.; Buse, G.; Bourenkov, G. P.; Bartunik, H. D.; Huber, R.; Than, M. E. *EMBO J.* **2000**, *19*, 1766–1776.
- (16) Tsukihara, T.; Aoyama, H.; Yamashita, E.; Tomizaki, T.; Yamaguchi, H.; Shinzawa-Itoh, K.; Nakashima, R.; Yaono, R.; Yoshikawa, S. *Science* **1996**, *272*, 1136–1144.
- (17) Farver, O.; Chen, Y.; Fee, J. A.; Pecht, I. *FEBS Lett.* **2006**, *580*, 3417–3421.
- (18) Liu, B.; Chen, Y.; Doukov, T.; Soltis, S. M.; Stout, C. D.; Fee, J. A. *Biochemistry* **2009**, *48*, 820–826.
- (19) Tiefenbrunn, T.; Liu, W.; Chen, Y.; Katritch, V.; Stout, C. D.; Fee, J. A.; Cherezov, V. *PLoS One* **2011**, *6*, e22348.
- (20) Wallace, D. C. *Science* **1999**, *283*, 1482–1488.
- (21) Zee, J. M.; Glerum, D. M. *Biochem. Cell Biol.* **2006**, *84*, 859–869.
- (22) Collman, J. P.; Ghosh, S. *Inorg. Chem.* **2010**, *49*, 5798–5810.
- (23) Collman, J. P.; Ghosh, S.; Dey, A.; Decreau, R. A.; Yang, Y. J. *Am. Chem. Soc.* **2009**, *131*, 5034–5035.
- (24) Kieber-Emmons, M. T.; Li, Y. Q.; Halime, Z.; Karlin, K. D.; Solomon, E. I. *Inorg. Chem.* **2011**, *50*, 11777–11786.
- (25) Verkhovskiy, M. I.; Jasaitis, A.; Verkhovskaya, M. L.; Morgan, J. E.; Wikström, M. *Nature* **1999**, *400*, 480–483.
- (26) Szundi, I.; Funatogawa, C.; Fee, J. A.; Soulimane, T.; Einarsdottir, O. *Proc. Natl. Acad. Sci. U. S. A.* **2010**, *107*, 21010–21015.
- (27) Farver, O.; Wherland, S.; Antholine, W. E.; Gemmen, G. J.; Chen, Y.; Pecht, I.; Fee, J. A. *Biochemistry* **2010**, ASAP.
- (28) Chang, H. Y.; Choi, S. K.; Vakkasoglu, A. S.; Chen, Y.; Hemp, J.; Fee, J. A.; Gennis, R. B. *Proc. Natl. Acad. Sci. U. S. A.* **2012**, *109*, 5259–5264.
- (29) Zimmermann, B. H.; Nitsche, C. I.; Fee, J. A.; Rusnak, F.; Munck, E. *Proc. Natl. Acad. Sci. U. S. A.* **1988**, *85*, 5779–5783.
- (30) Popovic, D. M. *Amino Acids* **2013**, *45*, 1073–1087.
- (31) Fadda, E.; Yu, C. H.; Pomes, R. *Biochim. Biophys. Acta* **2008**, *1777*, 277–284.
- (32) Siegbahn, P. E. M.; Blomberg, M. R. A. *Dalton Trans.* **2009**, 5832–5840.
- (33) Blomberg, M. R. A.; Siegbahn, P. E. M. *Mol. Phys.* **2010**, *108*, 2733–2743.
- (34) Blomberg, M. R. A.; Siegbahn, P. E. M. *Biochim. Biophys. Acta* **2012**, *1817*, 495–505.
- (35) Chang, H. Y.; Hemp, J.; Chen, Y.; Fee, J. A.; Gennis, R. B. *Proc. Natl. Acad. Sci. U. S. A.* **2009**, *106*, 16169–16173.
- (36) Smirnova, I.; Reimann, J.; von Ballmoos, C.; Chang, H. Y.; Gennis, R. B.; Fee, J. A.; Brzezinski, P.; Adelroth, P. *Biochemistry* **2010**, *49*, 7033–7039.
- (37) Han Du, W.-G.; Noodleman, L. *Inorg. Chem.* **2013**, *52*, 14072–14088.
- (38) Klamt, A.; Schüürmann, G. *J. Chem. Soc., Perkin Trans. 2* **1993**, 799–805.
- (39) Klamt, A. *J. Phys. Chem.* **1995**, *99*, 2224–2235.
- (40) Klamt, A.; Jonas, V. *J. Chem. Phys.* **1996**, *105*, 9972–9981.
- (41) Pye, C. C.; Ziegler, T. *Theor. Chem. Acc.* **1999**, *101*, 396–408.
- (42) *Amsterdam Density Functional Software*; SCM, Theoretical Chemistry, Vrije Universiteit: Amsterdam, The Netherlands, <http://www.scm.com>.
- (43) te Velde, G.; Bickelhaupt, F. M.; Baerends, E. J.; Guerra, C. F.; Van Gisbergen, S. J. A.; Snijders, J. G.; Ziegler, T. *J. Comput. Chem.* **2001**, *22*, 931–967.
- (44) Lanne, B.; Vanngard, T. *Biochim. Biophys. Acta* **1978**, *501*, 449–457.
- (45) Sousa, F. L.; Verissimo, A. F.; Baptista, A. M.; Soulimane, T.; Teixeira, M.; Pereira, M. M. *Biophys. J.* **2008**, *94*, 2434–2441.
- (46) Jhurry, N. D.; Chakrabarti, M.; McCormick, S. P.; Holmes-Hampton, G. P.; Lindahl, P. A. *Biochemistry* **2012**, *51*, 5276–5284.
- (47) Hallen, S.; Nilsson, T. *Biochemistry* **1992**, *31*, 11853–11859.
- (48) Bonin, J.; Costentin, C.; Louault, C.; Robert, M.; Saveant, J. M. *J. Am. Chem. Soc.* **2011**, *133*, 6668–6674.
- (49) Zaslavsky, D.; Smirnova, I. A.; Adelroth, P.; Brzezinski, P.; Gennis, R. B. *Biochemistry* **1999**, *38*, 2307–2311.
- (50) Zaslavsky, D.; Smirnova, I. A.; Brzezinski, P.; Shinzawa-Itoh, K.; Yoshikawa, S.; Gennis, R. B. *Biochemistry* **1999**, *38*, 16016–16023.
- (51) Han, W.-G.; Noodleman, L. *Inorg. Chem.* **2011**, *50*, 2302–2320.
- (52) Ullmann, G. M.; Noodleman, L.; Case, D. A. *J. Biol. Inorg. Chem.* **2002**, *7*, 632–639.
- (53) Lewis, A.; Bumpus, J. A.; Truhlar, D. G.; Cramer, C. J. *J. Chem. Educ.* **2004**, *81*, 596–604.
- (54) Lewis, A.; Bumpus, J. A.; Truhlar, D. G.; Cramer, C. J. *J. Chem. Educ.* **2007**, *84*, 934.
- (55) Tissandier, M. D.; Cowen, K. A.; Feng, W. Y.; Gundlach, E.; Cohen, M. H.; Earhart, A. D.; Coe, J. V.; Tuttle, T. R. *J. Phys. Chem. A* **1998**, *102*, 7787–7794.
- (56) Zhan, C. G.; Dixon, D. A. *J. Phys. Chem. A* **2001**, *105*, 11534–11540.